Ferroelectric and Ferromagnetic Alloy Clusters in Molecular Beams

A Thesis
Presented to
The Academic Faculty

by

Shuangye Yin

In Partial Fulfillment
of the Requirements for the Degree
Doctor of Philosophy

School of Physics
Georgia Institute of Technology
August 2006

Ferroelectric and Ferromagnetic Alloy Clusters in Molecular Beams

Approved by:

Professor Walter A. de Heer, Advisor
School of Physics
Georgia Institute of Technology

Professor Edward H. Conrad
School of Physics
Georgia Institute of Technology

Professor Phillip First
School of Physics
Georgia Institute of Technology

Professor Brian Kennedy
School of Physics
Georgia Institute of Technology

Professor Robert L. Whetten
Department of Chemistry and Biochemistry
Georgia Institute of Technology

Date Approved: May 9, 2006

To my parents and to my wife.

ACKNOWLEDGEMENTS

I first want to thank my advisor Dr. Walter A. de Heer. In the last five years, he gives me intensive training as a physicist. His insight in physics, research styles and diligence all provide good examples for my future career. I will benefit from his various suggestions in every detail of the scientific activities.

I also enjoy so many years of collabrations with Xiaoshan Xu and Ramiro Moro. We finished incredibly difficult jobs together. I am glad that Anthony Liang and John Bowlan joined this lab and made significant contributions.

I appreciate the time my committee members spent on my thesis, as well as the suggestions and question about this work. I want to thank Dr. Kennedy for valuable discussions and recommendations. I also benefit from talks with Dr. Whetten, Dr. First, Dr. Conrad, Dr. Berger, Dr. Landman, Dr. You, Dr. Sa De Melo and and Dr. Fox.

During my study in Georgia Tech, I received assistances from Judy Melton, Kathy Hardwick, Nancy Baggett, Debbie James, Patrica Dixon, Kelvin Carter and Scott Centers. Suport from the machine shop comes from Leon Halverson, Sam Mize and Norman Scott.

Most importantly, my family and friends are always standing behind me. Without their support, I would have never finished this thesis.

TABLE OF CONTENTS

LIST OF TABLES

LIST OF FIGURES

LIST OF SYMBOLS

amu	mass unit, 1 amu = 1.66053886 $\times 10^{-27}$kg
B	magnetic field
D	debye, unit of dipole moment, 1 D = 3.336 $\times 10^{-30}$ coulomb meter
d	electron spill-out distance
DOS	density of states
d_z	deflection in $\hat{\mathbf{z}}$ direction
E	electric field or energy
eV	electronic volt, unit of energy, 1 eV = 1.60 $\times 10^{-19}$ J
E_F	Fermi energy
nm	nanometer, 1 nm = 10^{-9} meter
excimer	excited dimer, used in excimer laser
IP	ionization potential
$I(x)$	deflection profile, intensity distribution at deflection x
K	Kelvin, unit of temperature
k_B	Boltzmann constant, $1k_B = 1.38^{-23}J/K$
m	mass of the cluster
M	number of secondary atoms
meV	unit of energy, 1 meV = 0.001 eV
N	number of primary atoms
n	number of valence electrons or number of atoms
P_N	dipole moment of Nb_N
PSTOFMS	position-sensitive time-of-flight mass spectrometer
R	radius
T	tesla, unit of magnetic field
T	temperature
T_c	superconducting transition temperature

TOF	time of flight
torr	unit of pressure, 1 torr = 133 pascal
v	volume or speed of the cluster
V_d	high voltage applied on electric deflection plates
x	deflection of a cluster or solute concentration
x_0	maximum deflection of an dipole by electric field
α	polarizability
δ	spacing between single-electron levels
δm	mass differences
Δ_{BCS}	energy gap of superconductor or in BCS theory
Δ_{NC}	energy gap of Nb clusters
Δ_P	parity gap, defined on small superconducting particles
ϵ_0	permittivity of vacuum (8.85×10^{-12} F/m)
μ	magnetic moment per atom
μ_0	total magnetic moment
μ_B	Bohr magneton, unit of magnetic moment, $1\mu_B = 9.27^{-24}$ J/T
ρ	Density of states
Å	angstrom, unit of length, 1 Å = 10^{-10} m

SUMMARY

Ferroelectric and ferromagnetic alloy clusters are produced and studied in molecular beams. Nb clusters doped with 1-3 impurity atoms are ferroelectric with low transition temperatures. The alloy clusters with an even number of valence electrons have larger dipole moments than those with odd number of valence electrons. The ferroelectricity is suppressed by magnetic impurities or thermal excitations, and is enhanced by Au and Al doping. The observations strongly suggest that electron-pairing interactions exist in Nb clusters, which indicates Cooper pairing in clusters. The magnetic moments of Co clusters doped with small fraction of Mn,V and Al are studied and compared with those of the bulk alloys. CoMn alloy clusters have enhanced average magnetic moments with Mn doping, which is opposite to the behavior of bulk CoMn. CoV and CoAl alloy clusters behave similarly to their bulk counterparts. We explain the experimental results using the virtual-bound-state model. Finally, the magnetic properties of BiMn clusters are studied in molecular beams. The Mn local moments are found to couple ferromagnetically or ferrimagnetically depending on the composition of the clusters.

CHAPTER I

INTRODUCTION

1.1 Atomic Clusters

According to Webster, a cluster is defined as "a number of similar individuals that occur together". Depending on the elements that make up the clusters, these could be stellar clusters, computer clusters, cell clusters, etc. In this work we study atomic clusters which are aggregates made of two to several millions of atoms of the same or different elements. The typical size range of atomic clusters is from 0.1 nm to 10 nm.

In atomic clusters, electrons not only bind atoms together but also determine most properties of the clusters. Therefore, the work in this thesis relies heavily on an understanding of the electronic structure of atomic clusters and how these structures connect to the observed magnetic and electric properties.

1.2 Why Study Clusters

Systematic studies of clusters in molecular beams greatly benefited from the invention of the seeded supersonic cluster source in 1968 [113] and the laser vaporization source in the 1980's [38]. Now it is possible to make clusters of almost any element. There are many reasons why these small objects are interesting.

Clusters connect the properties of atoms with those of the bulk. A single atom has totally different properties from a bulk sample made of 10^{23} such atoms. For example, bulk niobium is metallic, and becomes superconducting at low temperatures, but these properties do not apply for a single Nb atom. Understanding emergent phenomena in a bulk material is not easy because of the huge number of atoms and electrons and the complex interactions involved. Even if one could write down equations to describe all 10^{23} atom, it would not help to understand the emergent phenomena [10].

A relevant question is "what is the smallest number of atoms required to exhibit bulk

properties?". Experimentally, by looking at the emerging properties as size increases, one can understand them better.

Originally it was thought that small metal clusters are exotic and every cluster is essentially unique. After the discovery of the electronic shell structure in alkali clusters [76], the intrinsic connections between the different sizes become clear. Ionization potential (IP) measurements on sodium [141], copper [73] and silver clusters [4] revealed the IPs gradually decrease as a function of increasing size and finally reach the work function of the bulk. Similar trends are found in the polarizabilities of alkali clusters [75]. Further experiments have shown that many properties of the bulk manifest themselves in small clusters as well, such as ferromagnetism [18] and certain phase transitions [119, 134].

On the other hand, clusters also exhibit unique properties that are different from the bulk. Firstly they have large surface to volume ratio. The ratio scales with the cluster size as $N^{-2/3}$, where N is the number of atoms in the clusters. For a typical cluster made of 1000 atoms, about 40% of the atoms are on the surface. The atoms on the surface have dangling bonds and smaller coordination numbers, which usually makes them more chemically reactive. Many clusters are found to be good catalysts, e.g, gold clusters [117]. Bulk gold is an essentially non-reactive noble metal. However small gold clusters on the surface of magnesium oxide can act as an extremely good catalyst able to catalyze CO oxidation at temperatures as low as 140 K [84]. Clusters of ferromagnetic elements such as iron, cobalt and nickel show enhanced magnetic moments as a result of reduced coordination numbers. [18].

From the electronic structure point of view, electrons confined to small volume have large level spacings. Assuming uniformly spaced electronic levels, then the level spacing is $\delta = E_F/N$ [81]. Assume that the Fermi energy is $\sim$ 10 eV, for a cluster of 1000 electrons, $\delta \sim$ 300 K. This means that the discreteness of electronic states is becoming important at this size range at room temperatures. In alkali clusters, electronic levels are organized in an electronic shell structure as a result of delocalized electrons moving in a spherical potential well [76, 31]. The electronic shell structure has a significant effect on properties of simple metal clusters [31, 65]. Superconductivity is also affected. P. W. Anderson predicted

[8] that pairing gap would vanish when the level spacing becomes comparable with the bulk superconducting gap. But more recent calculations show that the effect might be the opposite; the gap would become even larger at small sizes [92, 118, 104].

There is a growing interest in using super stable clusters as building blocks ("super-atoms") for new materials [126, 136, 14, 99]. A well known example of this is the fullerene cluster, C_{60} [80]. Because of their perfect symmetry and stability C_{60} clusters can be produced with high yield, which enables synthesis of C_{60} based materials [126]. Other kinds of stable clusters have also been proposed. Clusters with closed electronic shell and icosahedral packing are found to be ultra stable such as Al_{13}^- [14], $Al_{12}X$ (X = Ge, Sn, Pb) [86] and $Pb_{12}Al^+$ [99]. It has been suggested that these superatoms will make a whole new family of functioning material with novel properties.

1.3 Cluster Experiments

Clusters can be studied in both gas phase or after being deposited on substrate. In these environments they are called "free clusters" and "supported clusters", respectively.

1.3.1 Free Clusters

In the gas phase, clusters are produced and detected in a vacuum chamber. The clusters form a cluster beam or are stored in ion traps and clusters of different sizes are separated by mass spectrometers. The typical methods used to study them include magnetic or electric deflection [94, 95], optical spectroscopy [35], photofragmentation [99, 119], photoelectron spectroscopy [86, 141], electron diffraction [44], and collision/reaction [100], etc. With free clusters, it is difficult to manipulate and measure a single cluster, and their properties are derived from measurements averaged over an ensemble of similarly prepared clusters.

Free clusters are ideal for fundamental research because they may be sized selected and do not interact with substrate or other unwanted contaminants, so that the intrinsic properties of the clusters are measured. Comparison with theory is much easier since interactions with substrates are not usually included in the calculations. Experimental techniques are limited since free clusters are in gas phase and standard microscopic methods

used in condensed matter and surface physics [58] are not applicable or are very difficult to implement.

1.3.2 Molecular Beam Deflection of Clusters

The work in this thesis is focused on free clusters studied in molecular beams. More specifically, we study the magnetic and electric properties of clusters by measuring beam deflection when they are passed though an inhomogeneous magnetic and/or electric field [83, 51, 96] and their magnetic or electric moments interacts with the fields.

Magnetic deflection of molecular beam date back to Stern-Gerlach (SG) experiments in the 1920s, where deflections of the different spin states of silver atoms splits the beam in inhomogeneous magnet. A first attempt to apply this method to potassium clusters was made by W. D. Knight in 1978 [77]. SG deflections of ferromagnetic clusters were first measured by looking at the on-axis intensity depletion of Fe clusters [29]. De Heer et al. first measured the complete deflection profiles of Fe clusters and revealed the spin-relaxation process involved in the deflection [34, 66, 145]. Using SG deflections, Billas et al have determined the magnetic moments of clusters from iron group (Fe, Co, and Ni) at the size range of about 20 to 1000 atoms. They found that magnetic moments of all the clusters are enhanced significantly compared with the bulk. For example, Co clusters can have a magnetic moment of as much as 2.4 Bohr magneton (μ_B) per atom while the magnetic moment per atom is only 1.6 μ_B in bulk Co. The average moments of those clusters decrease with increasing sizes and approach the bulk value at about several hundreds of atoms. The authors also determined the Curie temperatures of those clusters. Knickelbein [70] measured magnetic moments of Mn clusters, and found they become ferromagnetic or ferrimagnetic in clusters, while Mn is antiferromagnetic in the bulk. The measured magnetic moments of Mn clusters can be as large as 1.4 μ_B per atom and show size dependent oscillations where the moments are local minima for sizes 13 and 19 suggesting icosahedra packing. Cox et al. [28] found that Rh clusters become ferromagnetic with magnetic moments of about 0.8 μ_B while bulk Rh is paramagnetic. Gd clusters are found to be ferromagnetic in SG deflection [51, 39]. Gd clusters with 13 atoms were found to have canted magnetism, i.e.,

the directions of the atomic moments are not parallel to each other.

Using the electric deflection, the polarizability of sodium, potassium [75] and aluminum clusters [33] have been measured. The experiments show that the response of simple metal clusters to an external electric field is similar to that of a small metal sphere, except that the electron clouds spill out of the surface of ionic background [13] and this accounts for a large fraction of the polarizability at small sizes.

The electric deflections of Nb, V and Ta clusters at low temperatures are very different from those of simple metal clusters [94]. Large dipole moments are found for Nb clusters containing 3 to 200 atoms. The existence of dipole moments, which can be as large as a few Debye, is contradictory to the usual screening behavior of metals. More importantly, these dipole moments only appears are at low temperatures. As will be discussed in this thesis, the odd-even alternation of this effect as a function of cluster sizes suggests a relation to superconductivity.

1.4 Alloy Clusters in Molecular Beams

A further understanding of cluster properties can be obtained by doping the clusters with small amounts of impurity atoms. The response of the properties to "alloying" with various elements provides valuable information about their nature, as we show in this thesis. For example, we can increase the number of valence electrons or Fermi level by doping impurity atoms with excess electrons. We can also add strong magnetic interactions in the clusters by introducing a magnetic impurity atom with partially filled d or f orbitals. In this context, we apply the doping method to low temperature Nb clusters to better understand the electron pairing interaction and its connection to superconductivity in small clusters.

In addition, alloying is well known to introduce new interesting properties to bulk materials [130]. Permanent magnets made of alloys such as Neodymium magnets ($Nd_2Fe_{14}B$), Samarium-Cobalt magnets and Alnico magnets are widely used. The alloying behavior of clusters is an interesting and relatively unexplored field. Reduced size can have a profound effect on alloys, e.g., Co-Rh nanoparticles have been recently found to exhibit enhanced magnetism [151, 152].

Little work has been done on alloy clusters in molecular beams. SG deflection experiments have been performed on BiCo [55], DyTe and TyBi clusters [110]. There are also early works focusing on bimetallic clusters in the hope of finding super-stable species with special closed electronic and geometric shells [62].

In this thesis we are primarily interested in trends in alloy clusters, rather than special properties of a specific composition. We focus on the continuous modification of the properties of interest as a function of composition and size, and compare the behavior with that of the bulk.

In this context, we have made magnetic measurements on Co clusters doped with Mn, V and Al atoms. We find enhancement of the magnetic moment in CoMn clusters and we can explain all the doping behavior within the itinerant-band model. In addition, we study and discuss the magnetic properties of BiMn clusters, which provides a good example of magnetic impurities in non-magnetic cluster hosts.

CHAPTER II

EXPERIMENTAL METHODS

The apparatus to study clusters in molecular beam experiments can be divided roughly into three functioning parts: source chamber, deflection chamber, and detector chamber. The three chambers are differentially pumped to keep at pressures of about 10^{-2}, 10^{-7}, and 10^{-9} torr, respectively (Fig. 1). The clusters are produced in the source (Fig. 2) by pulsed laser ablation and form the cluster beam. The cluster beam is then collimated to a narrow width and it is deflected in the deflection chamber by an inhomogeneous magnetic or electric field. The deflected clusters enter the detector chamber where they are ionized using an excimer laser (193nm) and detected using a position-sensitive time-of-flight mass spectrometer (PSTOFMS). The digitized mass spectrum is stored in computer for analysis. The PSTOFMS measures the masses of the clusters and simultaneously records their deflections caused by the fields. From the deflections of the clusters, we determine the magnetic or electrical properties of all the clusters. The excimer can be replaced by an tunable OPO laser (Continuum Panther) to determine the ionization potentials of the clusters.

The processes are synchronized and repeated at 20 Hz, and are electronically controlled by three timing units. Data acquisition for single position-sensitive measurement typically takes several hours, but it includes data for all of the sizes (typically one hundred) in the beam.

2.1 Low Temperature Cluster Source

The alloy clusters are produced in a cryogenically cooled pulsed laser vaporization source, which is maintained at low temperature by attaching to a closed-cycle cryogenic refrigerator (Sumitomo SRDK CSW-71) and a feedback-controlled heating system (Lakeshore 321). (See Fig. 2 for schematic plot of the source.) High power laser pulses (Continuum Surelite I20, 355nm) are focused on an alloy target rod of about 2 mm diameter and of the desired

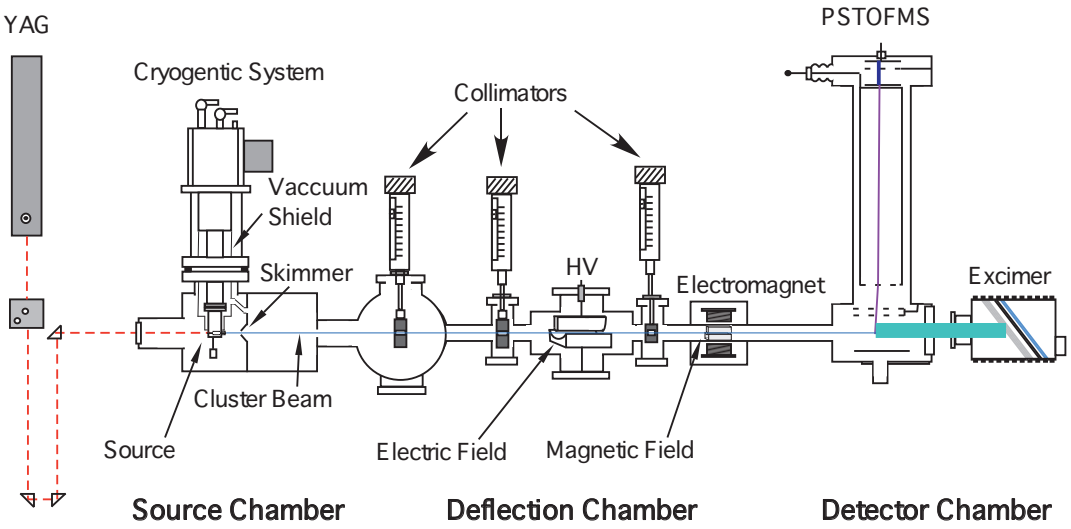

Figure 1: Schematic view of molecular beam deflection experiments. The clusters are produced in a laser-ablation source attached to closed-cycle cryogenic refrigerator (see Fig. 2 for details of the source). The cluster beam is subsequently collimated to a width of about 0.3 mm before it enters the inhomogeneous electric or magnetic field. The electric field is generated by applying a high voltage over a pair of curved electric plates; and the magnetic field is generated by a Stern-Gerlach magnet inside an electromagnet. At the end of the beam, the clusters are ionized by an excimer laser and are detected by the PSTOFMS, which simultaneously measures the masses and the deflections of the clusters.

chemical composition. A short and intense laser beam focused on the target surface can raise the local temperature to above the boiling temperature and create an atomic vapor [15, 96]. The vapor is cooled subsequently by a pulse of carrier gas. Helium gas is usually used in our experiments because it does not liquify at the lowest temperature in our experiments. Other carrier gases such as Ne, Ar and N_2 can also be used as carrier gases at higher temperatures. After formation, the clusters cool and equilibrate with the source [83, 96], and exit the nozzle to form a cluster beam. The excess carrier gas is removed from the beam by a skimmer at about 1.5 cm from the nozzle.

The carrier gas plays two roles in the formation of clusters [15]. First, it restricts the diffusion of vapor atoms, which limits the formation of clusters. Second, it helps to cool the atomic vapor, which is required in the formation of clusters. Cohesive energies in clusters are on the order of several eVs per atom. This energy release by addition of an atom to a cluster smaller than 7-14 atoms can raise the cluster temperature to above the melting point [15]. In order to have the cluster grow further, this heat needs to be removed quickly.

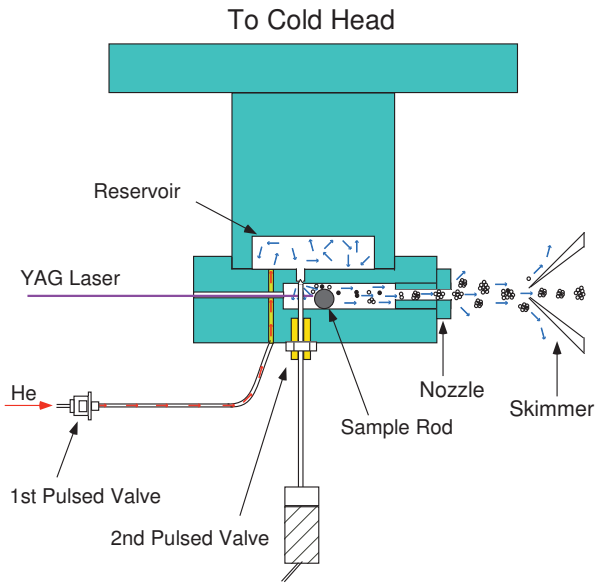

Figure 2: Schematic view of the cryogenic cluster source. The whole source body is mounted on the cold head of the cryogenic system and is covered with thermal shields. A short pulse of laser is focused on the sample rod sitting in the source cavity and generate an atomic vapor, which is subsequently cooled by a pulse of carrier gas (usually He) and condenses to form clusters. The clusters further grow and gain thermal equilibrium with the cold carrier gas and the source before exit from the nozzle and form a cluster beam. The residual carrier gas is removed from the beam by a skimmer sitting about 1.5 cm away from the nozzle. To pre-cool the carrier gas, a reservoir is built in the source body; the gas is injected into the reservoir by the first pulsed-valve and is kept for ∼30 ms to allow full equilibrium with the cold source body before it is released into the cavity by the second pulsed-valve.

Successive collisions of the cluster with cold carrier gas atoms can help to keep the cluster cold and help the production of clusters [83, 51]. The cooling efficiency in a laser ablation source is usually considered to be between a supersonic source and a gas aggregation source [15].

In order to have sufficiently cold carrier gas, a reservoir is built inside the source. The carrier gas is released into the reservoir though a pulsed valve and dewells there for about 30 ms to equilibrate with the cold source body [96] before it is ejected into the source cavity. Most surface of the source are enclosed in vacuum shields and pumped to about 10^{-4} torr (see Fig. 1). Only the minimum surface area is exposed to the relatively high pressure (10^{-2} torr) in the source chamber to prevent convective and conductive heat leaks. The temperature of the source is measured by a silicon diode (LakeShore 470) attached to the source.

Experiments confirm that the clusters produced from this source have speeds corresponding to the expected molecular beam's speed. The measured magnetic deflections are also consistent with a superparamagnetism model if the cluster temperature corresponds to the source temperature [145]. These observations indicate that the clusters produced in this source are in good thermal equilibrium with the source.

It is important to study clusters using a low temperature source. Since cluster speed scales as $1/\sqrt{T}$ with temperature, low temperature clusters can have lower speeds and therefore have larger deflections for the same field strength conditions, which provides better accuracy in molecular beam deflection experiments. More importantly, a low temperature source allows us to study cluster properties close to the vibrational and electronic ground states [51].

2.2 Electric and Magnetic Deflection of Cluster Beams

The second part in the apparatus is the deflection chamber, where the clusters are deflected by interacting with an inhomogeneous electric or magnetic field. The typical pressure in the deflection chamber is on the order of 10^{-7} torr, which corresponds to a mean free path of about 20 m for a cluster of 100 atoms. The width of the cluster beam is always checked to ensure no scattering by the background gas.

Before entering the inhomogeneous fields, the cluster beam is collimated to a width of about 0.3 mm. Narrow collimation is favorable because it not only provides better accuracy for measuring beam deflections but also improve the mass resolution in the position-sensitive mass spectrum.

The inhomogeneous magnetic and electric fields are all Rabi [108, 113] two-wired fields. The collimated cluster beam goes through the middle of the fields, where the field strength and gradient have little variation across the beam. As a cluster flies through a inhomogeneous field, the interaction of the magnetic or electric dipole moment with the field gradient will cause the cluster to deflect.

The magnetic and electric fields in our experiments are uniform along the cluster beam axis but have the most gradient on the horizontal direction perpendicular to the beam axis.

Only the deflections in this direction (which is assigned as **z** direction) are measured in our experiments.

2.2.1 Magnetic Deflection

For magnetic fields, the deflection of a cluster (d_z) is proportional to the average magnetization (M_{eff}) of the cluster during its flight through the magnetic field, which is determined by the following equation,

$$d_z = K\frac{M_{eff}\frac{dB}{dz}}{mv^2} \tag{1}$$

where K is the geometric factor of the apparatus, $\frac{dB}{dz}$ is the magnetic field gradient, and m and v are the mass and speed of the cluster. In experiments, M_{eff} can be deduced by measuring the deflection of the clusters if other parameters are known.

It is known that coupling of the magnetic moment to the rotations causes spin-relaxation-like effects so that the deflections are reduced and are only toward strong field direction [66]. It has been shown only recently that the relaxation is not really caused by the thermal motion of the spin inside a cluster but rather by an adiabatic change of the spin direction as a result of coupling of spin to other degrees of freedom [145]. The average magnetization of the ensemble of the clusters turns out to be the same as the thermodynamic average described by the Langevin equation:

$$M_{eff} = \mu_0\left(coth\frac{\mu_0 B}{k_B T} - \frac{k_B T}{\mu_0 B}\right) \tag{2}$$

where μ_0 is the total magnetic moment of the cluster, B is the magnetic field, k_B is Boltzmann constant, and T is the temperature of the cluster ensemble. In low field limit ($\mu_0 B/k_B T \ll 1$), it can be approximated as,

$$M_{eff} = \frac{\mu_0^2 B}{3k_B T} \tag{3}$$

.

By using Eq. 2 and 3, we can deduce the intrinsic value of the magnetic moment from the measured average magnetization M_{eff}.

High accuracy is especially important for studying magnetism of alloy cluster, since we are looking at changes of a few Bohr magnetons on top of a few hundred Bohr magnetons.

This requires accurate deflection measurements of within a few percent. In order to achieve such high accuracy, it is desirable to use narrowly collimated and intense cluster beams.

2.2.2 Electric deflection

For electric deflections, the Stern-Gerlach magnet is replaced by a pair of parallel brass plates and are applied with high voltage of up to 20 kV [96] (Fig. 1). The deflection by the electric field is similar to that by the magnetic field, which can be written as,

$$d_z = K\frac{D_{eff}\frac{dE}{dz}}{mv^2} \tag{4}$$

where D_{eff} is the electric dipole moment, and dE/dz [1] is the gradient of the electric field. Other parameters are the same as from the magnetic case. D_{eff} can be either an induced dipole moment or a permanent dipole moment.

An induced dipole of a metal cluster resemble to that of a small metal sphere, which is the result of collected responses of a free electron cloud to an external field. The electron cloud is shifted in the opposite direction of the external field to completely screen the electric field inside the clusters. The induced dipole moment is proportional to the external electric field,

$$D_{eff} = \alpha E \tag{5}$$

where α is the polarizability, and E is the electric field. The polarizability of a metal sphere is found to be proportional to volume, $\alpha = R^3$ in c.g.s. or $\alpha = 4\pi\epsilon_0 R^3$ in S.I., where R is the radius of the sphere and ϵ_0 is the permittivity of vacuum (8.85×10^{-12} F/m). The convenient unit used for the polarizability of cluster is Å^3 (in c.g.s.unit). For electric dipole moments at the atomic scale, the unit debye (D) is widely used, which is defined as 10^{-18} statcoulomb centimeter, or 3.336 $\times 10^{-30}$ coulomb meter in S.I. units.

For metal cluster polarizabilities, the spill-out effect [21, 13] has to be considered. The electron density extends beyond the ionic background by a small displacement d and the polarizability can be written as [122],

$$\alpha = (R + d)^3 \tag{6}$$

[1] The typical values are $E = 8 \times 10^6$ V/m and $dE/dz = 3.5 \times 10^9$ V/m^2

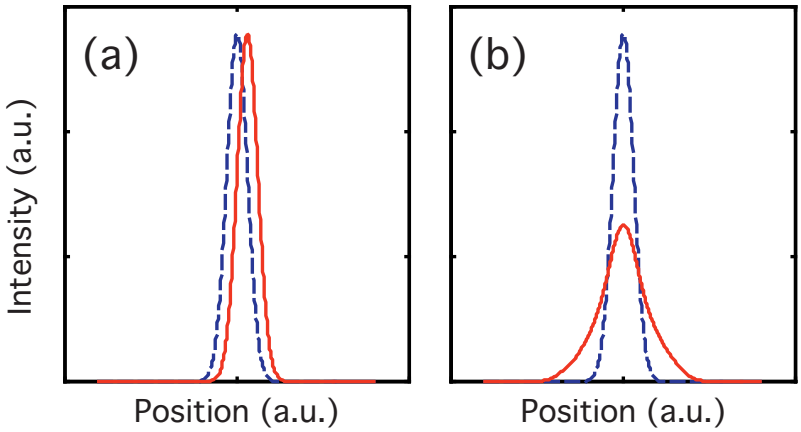

Figure 3: Schematic plots of electric deflection profiles (solid lines) of (a) a polarizable cluster and (b) a cluster with a permanent electric dipole moment fixed on axis. The beam profiles without electric field are also shown for comparison (dashed lines). The deflection profile is single-sided shift for normal polarizable clusters and is broadened for clusters with dipole moments. The deflection profile of fixed dipole moment is based on the model from Dugourd et al. [40].

Eq. 6 gives a reasonable first order description of polarizability of simple metal clusters.

For a polarizable cluster, the induced dipole is always on the same direction as the external field, which causes a deflection toward the strong field direction. Consequently, all clusters of the same size will have the same deflection independent of the rotational states. The deflection profile of a polarizable cluster is ideally a shifted peak (Fig. 3a). In practice, it is also slightly broadened, due to the finite cluster beam width and the field inhomogeneity. In contrast, the deflection of a permanent dipole in electric field is more complicated [16, 40, 7]. In a classical picture, a cluster with a electric dipole fixed on one axis will have the motion of a Lagrangian top. It is also well accepted that, as the rotating top enters the electric field, its motion will change adiabatically, which conserves all the angular momentum [16, 40]. By solving the adiabatic equations, the average projection of the dipole moment in one direction can be calculated. It turns out that the average projection depends on the initial dipole direction and rotation of the cluster, so that the deflection is not always the same for the same clusters. Experimentally, the accumulated measurement will have a broad distribution of deflections (see Fig. 3b). By studying deflection profiles, one can infer the intrinsic moments in the clusters [95] [40].

2.3 Time-of-flight Mass Spectrometer

At the end of the beam (Fig. 1), all the clusters are ionized using an ArF excimer laser (Lambda Physik Optex, 193nm) and detected in a PSTOFMS [32]. In the PSTOFMS, the time-of-flight is not only determined by the mass but also partially by the position of the clusters. As a result, the mass resolution is traded off for position-sensitivity using appropriately tuned electric field. The typical relation between TOF, mass (m) and position of a cluster (x) can be written as,

$$TOF = (c_1 + c_2 x)\sqrt{m} \tag{7}$$

where c_1 and c_2 are parameters that is determined by geometry and voltages. By adjusting voltages we can set the position-sensitivity c_2 to zero and the TOF functions in the high resolution mode. Setting voltages away from high resolution mode will make the TOF position-sensitive, and the position-sensitivity can also be tuned for experimental purposes. Experimentally the TOF is digitized using a multiscaler (FAST ComTec, 7886) running at 1.95 GHz, and every channel corresponds to a TOF of $\frac{1}{1.95\times10^9}$ sec. Expressing TOF in channels, deflection in mm, and mass in amu, then in the position-sensitive mode, c_1 and c_2 parameters are 1762.2 and 0.75, respectively. Since the deflection of the beam is usually less than a few mm, the second term in Eq. 7 is much smaller than the first term, the position-sensitive condition is very close the that of the high-resolution condition with only a small modification.

From Eq. 7, mass peaks with mass difference δm are separated roughly by $\frac{c_1}{2\sqrt{m}}\delta m$ in TOF. The separation becomes smaller at larger masses. At the same time, the widths of the peaks (σ) are determined by the collimation. According to Eq. 7 the spreading of the mass peaks in TOF scales as $c_2\sigma\sqrt{m}$, which increases with increasing size. These two factors limit the resolution of PSTOFMS for large clusters.

For pure clusters, the mass resolution is usually not a problem, because mass separation between different cluster peaks is the mass of one atom, which is relatively large. For example Nb clusters have mass separation of 93 amu, and Nb clusters with up to 4000 atoms can still be separated in position sensitive mode.

2.3.1 Mass Spectrum of Alloy Clusters

The resolution is a concern for alloy clusters, because the mass differences between alloy clusters are much smaller. Let us only consider the binary alloy cluster $A_{n_1}B_{n_2}$, the mass of this cluster is $m = n_1m_1 + n_2m_2$, where m_1 and m_2 are the atomic mass of A and B, respectively. Consider dn to be the number of possible values of n_1 and n_2 in the mass range $m < n_1m_1 + n_2m_2 < m + dm$. It can be shown that

$$dn = \frac{m}{m_1m_2}dm \tag{8}$$

In order to have all the peaks resolved, there should be less than one mass peak per amu. Give $dm = 1$ amu and $dn = 1$, the upper limit of maximum mass below which all the alloy peaks can be resolved is (all masses are in units of amu)

$$m_{max} = m_1m_2 \tag{9}$$

Usually, it is not necessary to resolve all the alloy cluster peaks. Because of statistics during the formation of alloy clusters, some clusters are less likely formed and do not contribute significantly to the mass spectrum. For example in experiments using the alloy $Co_{0.8}Mn_{0.2}$ as source material, the possibility to produce a Co_5Mn_{20} cluster is about 10^{-10} times smaller than a $Co_{19}Mn_5$ cluster. Even though these two clusters have nearly the same mass (1393.5 amu and 1394.4 amu, respectively); this is not a problem for data analysis.

Mathematically, the possibility to produce $A_{n_1}B_{n_2}$ is a binomial distribution:

$$p(n_1 = n - n_2, n_2) = n!(1 - x)^{n_1}x^{n_2}/n_1!n_2! \tag{10}$$

where x is the atomic concentration of element B in the atomic vapor. The sum over all position n_2 gives $\sum p(n_2) = 1$.

To calculate average of n_2, which is defined as $\sum p(n_2)n_2$, we introduce the generating function as

$$f(s,t) = (s + t)^n = \sum_{n_2} \frac{n!}{n_2!(n - n_2)!}s^{n-n_2}t^{n_2} \tag{11}$$

then we have

$$< n_2 >= \sum_{n_2} \frac{n!}{n_2!(n - n_2)!}s^{n-n_2}t^{n_2}n_2 = t\frac{\partial}{\partial t}f(s,t)|_{s=1-x,t=x} \tag{12}$$

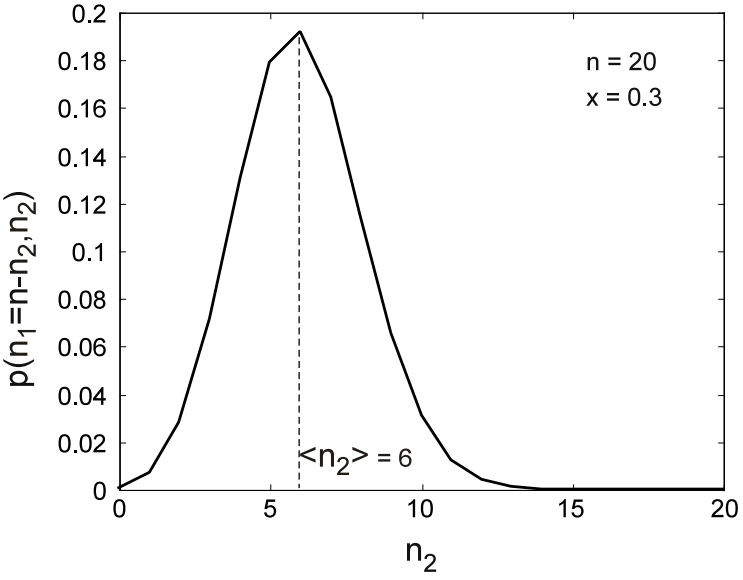

Figure 4: Binomial distribution of $p(n_1 = n - n_2, n_2)$ versus n_2. n is the total number of atoms; n_1 and n_2 are the numbers of atoms from element A and element B, respectively. x is the fractional concentration of B atoms in the atomic vapor. The maximum and average distribution is around nx, same as the stoichiometric composition in the atomic vapor. The probability to produce cluster with concentration away from that average is reduced.

while

$$t\frac{\partial}{\partial t}f(s,t) = t\frac{\partial}{\partial t}(s+t)^n = n(s+t)^{n-1}t \tag{13}$$

let $s = 1 - x$ and $t = x$ we get the average of n_2 to be

$$< n_2 >= nx \tag{14}$$

To the second order, the same procedure gives the width of the distribution of n_2

$$\sqrt{< (n_2 - < n_2 >)^2 >} = \sqrt{nx(1-x)} \tag{15}$$

The average value of n_2 equals nx, hence the atomic distribution of these two elements in clusters is on average the same as that in the sample rod. On the other hand, the width of the n_2 distribution scales as $\sqrt{n}$ and the fluctuation of concentration n_2/n will decrease as $\frac{1}{\sqrt{n}}$. That means for larger sizes, the produced clusters tend to have the same stoichiometric composition as that of the sample rod.

The distribution of n_2 is proportional to the distribution of mass. When the standard deviation of the mass of clusters with n atom is larger than half of the mass spacing between

next cluster sizes, the alloy peaks are not resolvable. In this situation, $\Delta m\sqrt{nx(1-x)} > 0.5m_0$, where m_0 is the average atomic mass. This gives the critical size to be $n_c = \frac{m_0^2}{4x(1-x)(\Delta m)^2}$. For a $Co_{0.5}Mn_{0.5}$ sample, $\Delta m = 4$ amu, $m_0 = 57$ amu, $x = 0.5$, we find $n_c = 218$.

Due to this constraint, we always limit our studies on relatively small clusters (< 100 atoms), where the mass resolution is good and clusters are well separated. The alloy clusters we studied here are always checked first by high-resolution TOF to ensure the various mass peaks are sufficiently resolved.

Another limitation on alloy experiments comes from isotopes. The presence of isotopes plays the same role as different element species. This is the reason all of the alloy clusters studied in this work only containing elements with only one natural isotope or with one dominant isotope. For example, vanadium has two natural isotopes of masses of about 51 amu and 50 amu. The 50 amu isotope has natural abundance of only 0.2%. Consequently, clusters containing 100 vanadium atoms has mass broadening of only 2% amu according to Eq. 15, which is well acceptable for PSTOFMS.

We also have developed Matlab programs that can identify alloy cluster peaks in the mass spectrum based on their masses. In most cases, it is sufficient to discern the composition only by mass. In other cases, the ambiguity is eliminated by comparing the mass spectrum with the predicted mass spectrum based on Eq. 11. An example of the alloy mass spectrum is shown in Fig. 5 for Au_NCo_M clusters.

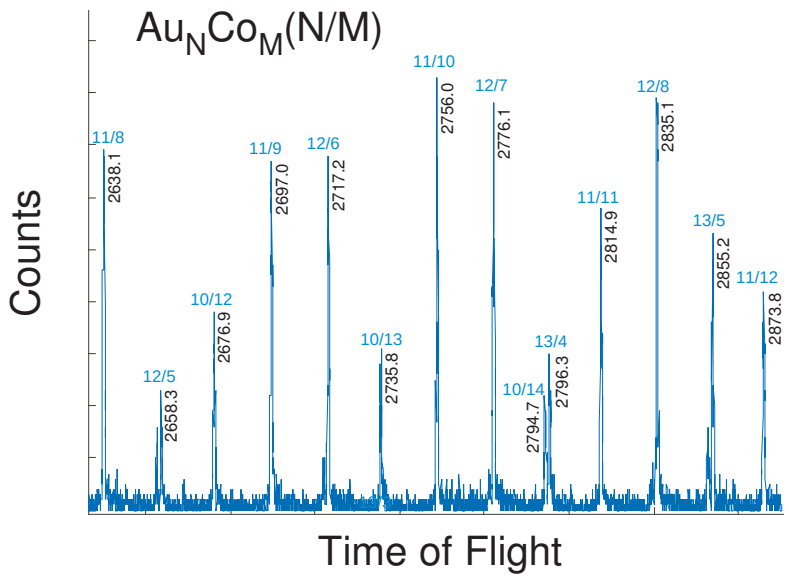

Figure 5: Time-of-flight mass spectrum example of Au_NCo_M clusters. The masses of the peaks are determined from the TOF using Eq. 7, which are shown next to the peaks (in units of amu). The smallest spacing between cluster peaks is only 1.6 amu. The cluster compositions can be determined from their masses and from intensity distributions, which are marked above the peaks as N/M.

CHAPTER III

FERROELECTRIC ALLOY CLUSTERS

3.1 Introduction

Superconductivity is a low temperature phenomenon of some materials characterized by the disappearance of resistance and exclusion of magnetic fields (Meissner effect). This phenomenon, has been extensively studied since its discovery [128].

The first microscopic theory to successfully explain superconductivity is due to Bardeen, Cooper and Schrieffer (BCS) [11]. In BCS theory, two electrons near the Fermi surface, and with opposite spins and momenta attract each other while their motion is coupled to the lattice vibrations (electron-phonon coupling). Cooper [27] showed that such an attractive interaction can result in formation of a bound state below Fermi level ("Cooper pair"). The pair formation causes an instability of the normal electrons near the Fermi surface and a condensed ground state (BCS ground state) is formed. There is a gap Δ_{BCS} between the ground state and next excited state. Assuming that all the electrons near the Fermi surface have attractive pairing interactions, the energy gap is found to be

$$\Delta_{BCS} = 2\hbar\omega_D \exp\left[-\frac{1}{\rho V}\right] \tag{16}$$

where ω is the Debye frequency, ρ is the density of states at Fermi level, and V is the average strength of the attractive interaction. The electron pairs move frictionlessly even with the presence of scattering, since it requires at least $2\Delta_{BCS}$ energy to break a Cooper pair and to make an excitation of two quasi-particles. This is the origin of the zero resistance at low temperatures.

The superconductivity will disappear when electron pairs are broken by thermal motion. The transition temperature of superconductivity (T_c) is related to the energy gap by

$$2\Delta_{BCS} = 3.52 k_B T_c \tag{17}$$

.

Soon after the BCS theory, Bohr, Mottelson and Pines recognized that a similar pairing mechanism exists in nuclei as well [20], where attractive interactions between nucleons form BCS-like ground state. If there are an odd number of nucleons, then the last nucleon cannot participate in the condensate and will stay in a higher energy state above the gap. This successfully explains the odd-even alternation in the nuclear excitation spectra [20].

Metallic clusters and atomic nuclei share many similarities. They are both small confined fermionic systems. To the first order, they can both be successfully described as independent fermions moving in potential wells, which leads to shell models in both nuclei and metallic clusters [25]. This connection would raise the question that whether pairing interactions could also exist in metallic clusters.

It is usually thought that superconductivity cannot exist in small particles when the size is smaller than coherent length of the superconductor. On the other hand, when the spacing between electronic states (Kubo gap [81]), δ, is larger than the Δ_{BCS}, it will be ambiguous to tell if there exists a superconducting gap [8]. Experimentally, when the size of the superconductor is small (less than 100 nm), the traditional methods of probing superconductivity (zero conductance and Meissner effect) become extremely difficult.

Nevertheless, Ralph, Black and Tinkham [19, 112] were able to demonstrate experimentally an odd-even alternation in the tunneling spectra of Al grains, from which they deduced the superconducting gaps. They found that the superconducting gap decrease as the size of the grains decrease. It is worth noting that the size of the grains are much smaller than the coherence length of the bulk.

Theoretically the original BCS model has also been extended to be applicable to small systems. At small size, quantum fluctuation of the gap become important. Extra care has to be taken to deal with superconductivity in small systems. When $\delta \sim \Delta_{BCS}$, the superconducting gap cannot be distinguished from quantum level spacing. So Matveev et al. proposed using parity effect to describe superconductivity in nanoparticles. The parity effect is defined as the oscillation of the ground state energy $\Delta_P = E_{2N+1} - \frac{1}{2}(E_{2N} + E_{2N+2})$, where E_l is the ground state energy of small particle with l electrons. When applied to bulk, the definition gives $\Delta_P = \Delta_{BCS}$. After they correctly included the quantum fluctuation of

the order parameter in nanoparticles, they found that as the size decreases, the parity gap first weakens. After reaching a minimum at a certain size such that $\delta \sim \Delta_{BCS}$, it increases [92].

Von Delft et al. [22, 118] proposed that two types of pairing parameters can be used in small superconducting particles; they characterizes collective and the single-particle properties of the system, respectively. These two parameters all reduce to the bulk superconducting gap as the size increase [118].

It also has been predicted that in certain cases, the superconducting gap of clusters can even exceed the value of bulk. Ovchinnikov and Kresin calculated the pairing interaction in nanoclusters, they found when the electronic states are highly degenerate, for example in shell structure, superconducting pairing can be strengthened and a large increase in the transition temperature and other superconducting parameters is expected [104, 105].

Our work on Nb clusters was inspired by the possibility to have superconductivity in small Nb clusters. Nb has one of the largest superconducting transition temperature T_c of all the pure elements. Its T_c, 9.25 K, is close to what we can achieve using the low temperature cluster source. Our initial try was to find the Meissner effect from magnetic deflections. We found that Nb clusters do not show diamagnetic deflections [94, 95], but instead, show unusual electric deflections at low temperatures.

3.2 Ferroelectricity in Nb clusters

Here we present a brief description of the ferroelectricity of Nb clusters, more details can be found in Ref. [94] and [96].

As shown in the previous chapter, deflection of normal metal clusters are similar to that of classical metal sphere [31]. The external field is screened by relative shift of electron cloud with respect the ionic background. As a result, the induced dipole is always parallel to external field, and cause uniform deflection of the clusters toward the strong field direction.

Electric deflections on Nb clusters show that they deflected like normal metal clusters at room temperature, which is characterized as pure shift of deflection profiles toward strong field, without noticeable broadening (Fig. 6). With various deflecting voltages (V_d)

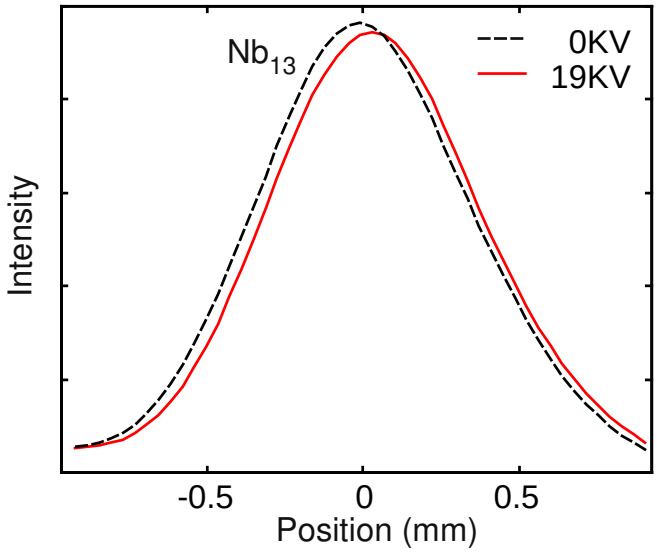

Figure 6: Deflection profile of Nb_{13} cluster at room temperature (300 K). With inhomogeneous electric field applied, the clusters are deflected uniformly toward the strong field direction, indicating a polarizable behavior. Clusters of other sizes have similar deflection behaviors at room temperature.

applied, the deflection is found to be proportional to V_d^2, consistent with what is expected for polarizable clusters (Eq. 4 and 5) [94].

When the Nb clusters are produced at 20 Kelvin, the deflection profiles dramatically deviate from that expected for normal metal cluster. A typical deflection profile of a cryogenic Nb cluster has a normal component and a ferroelectric component (Fig. 7, see also [94]). The normal component is polarizable and deflects proportional to V_d^2, which produces the slightly deflected central peak. The ferroelectric component produces large deflection tails and the extensions of the tails are found to be proportional to V_d [94], indicating permanent electric dipoles rather than induced dipoles. The tails are in both strong and weak field directions for small clusters, but they are primarily in strong field direction for large clusters.

These electric dipoles are found to occur only at low temperatures. The characteristic transition temperature below which the effect can develop is found to be to the order of 10 Kelvin, which is close to the superconducting transition temperature of Nb bulk. The same correlations are also found for V and Ta clusters [94].

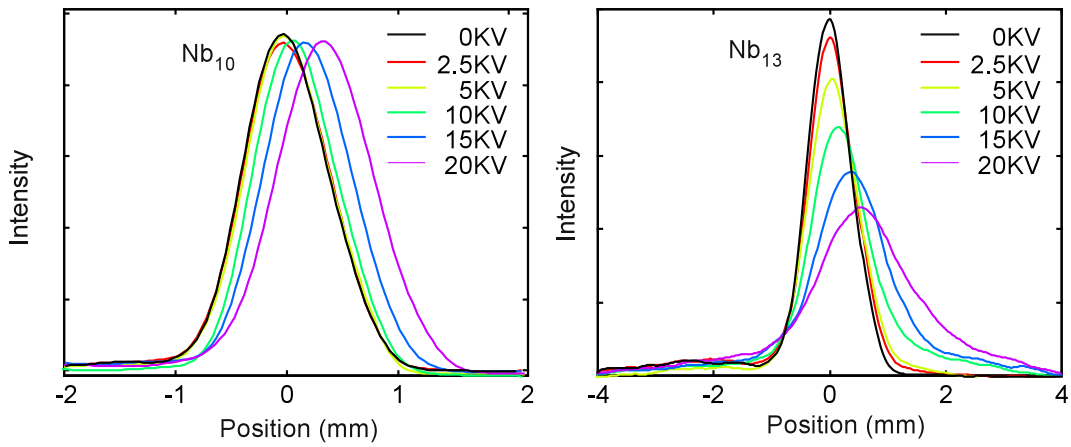

Figure 7: Deflection profiles of Nb clusters by various fields at 20 Kelvin. Each color line corresponds to different high voltage V_d applied on the electric plates. Most clusters at 20 Kelvin deflect similar as Nb_{13} (shown in the right panel), which is characterized by wings and reduced central peak in the deflection profile. This kind of deflection corresponds to existence of permanent electric dipole moments in those Nb clusters. Nb clusters at several special sizes, such as Nb_{10}, Nb_{15}, Nb_{17}, Nb_{19} and Nb_{22}, still deflects like normal polarizable clusters, an example of which is shown in the left panel for Nb_{10}. In this case, the average deflection is proportional to V_d^2. These clusters might have very higher symmetry that prevents formation of dipole moments.

The most striking feature of the ferroelectricity in Nb_N clusters is the odd-even alternation for large sizes ($N > 30$), i.e., all the Nb_N clusters with even N have larger dipole moments than their neighbor clusters with odd N (Fig. 8f). A Nb atom has a odd number of valence electrons (two 4s electrons and three 3d electrons) and the total number of valence electrons $n = 5N$, hence odd-even in N implies an odd-even numbered valence electrons. This observation implies a possible role of electron pairing in the ferroelectricity of Nb clusters.

The odd-even alternation is best shown by plotting all the normalized deflection profiles $I_N(x)$ in a color map as in Fig. 8 (a) and (b). The normalization is done in such a way that $I_N^{V_d=0}(0) = 1$. A vivid contrast is observed in the maximum intensities of $I_N(x_0)$, where $x_0 \approx 0.25$ mm because the average polarizability (α_N/N) of Nb clusters is essentially constant [94]. The Nb_N clusters with even N have smaller $I_N(x_0)$ more extensive tails, which show as "streaks" extending to the edge of the the detection window. At larger sizes, the deflections are mainly toward the strong field direction. There are a few Nb clusters, such as Nb_{10}, Nb_{15}, Nb_{17}, Nb_{19} and Nb_{22} that deflect like normal polarizable clusters at 20

K.

The reduction of the maximum intensity, $D_N = 1 - I_N(x_0)$, is due to the deflection of the dipoles, which provides valuable quantitative information about the magnitudes of the dipole moments. For measurements presented here, which were all performed under the same conditions, there is a empirical relation between D_N and the dipole moment of the cluster P_N,

$$P_N = \frac{N D_N (1 - 0.8 D_N)}{7(1 - D_N)}. \tag{18}$$

The relation, which approaches $\frac{N D_N}{7}$ for $D_N \to 0$, and $\frac{0.03N}{1-D_N}$ for $D_N \to 1$, provides reasonable estimates of P_N, for $N > 15$.

3.3 Alternative Interpretations

The observation of ferroelectricity in Nb clusters has inspired theoretical efforts on the origin of the ferroelectricity and the possibility of superconductivity in small clusters [104, 105, 5, 57, 6, 7, 43]. But the explanations are not uniform. Density functional calculations [6, 7] speculated that dipole moments of Nb_N clusters ($N < 15$) result from the asymmetry of the Nb cluster structures. The authors were able to find an correlation between dipole moments and their calculated asymmetry of small Nb clusters for $N < 15$. They, however, failed to explain the temperature dependence of the dipole moments, i.e., the dipole moments appear only at below certain transition temperatures T_G. Density functional calculations have also been extended to clusters containing up to 50 atoms, in order to explain the odd-even alternation in the ferroelectric response [43].

However, it is difficult to correctly include correlations in density functional calculations. The ground state structures also are difficult to optimize. These imperfection in calculations often cause erroneous result in cluster properties, even for simple metal clusters [31, 21]. Clearly more experiments were needed to clarify to the following questions regarding ferroelectricity in Nb clusters:

(1) Is it of structural origin or of electronic origin? The structural hypothesis says that the asymmetric positioning of ionic background causes electron density that cannot completely neutralize the positive charges, resulting in dipole moments, and electron pairing plays no

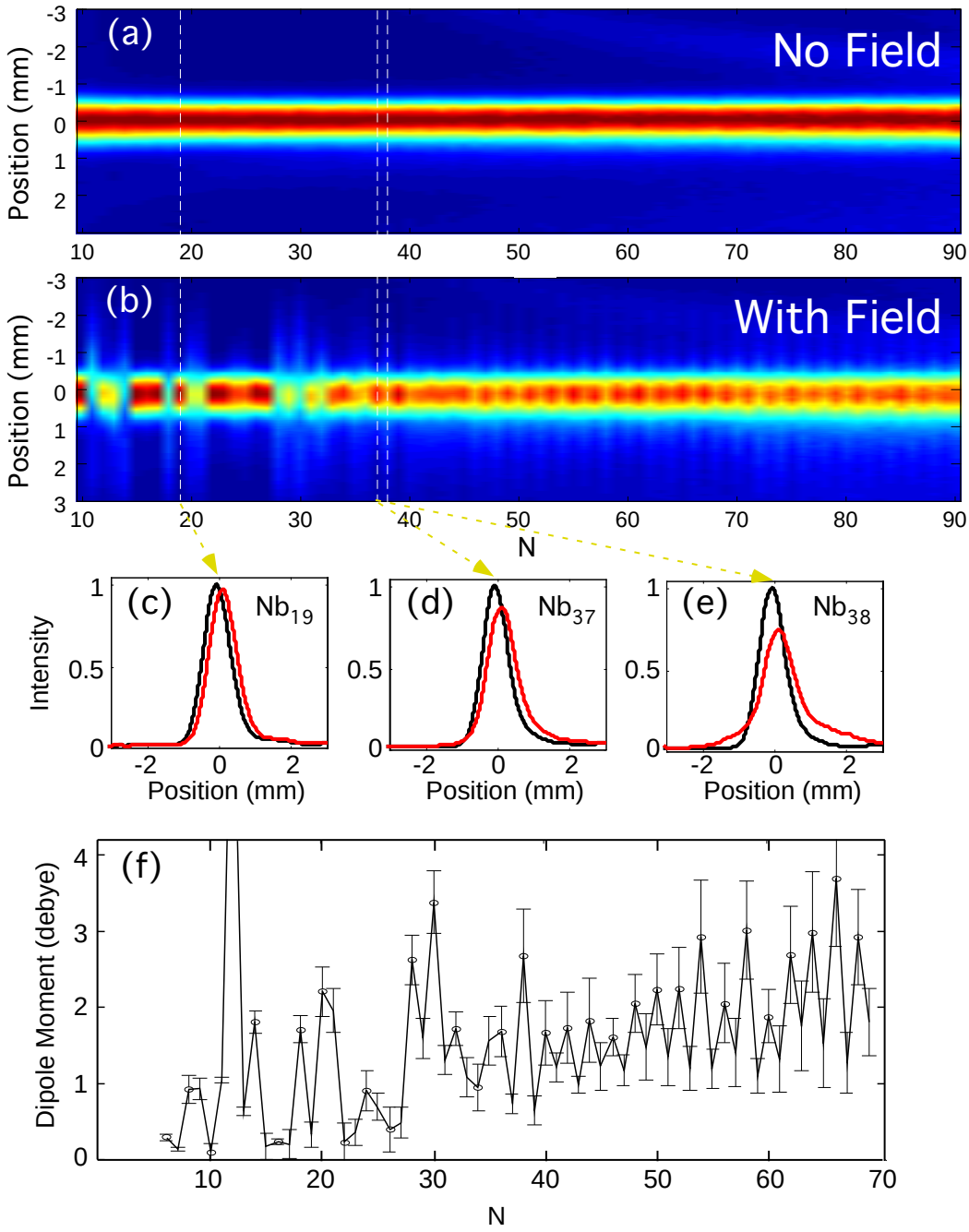

Figure 8: (a)(b) Deflection profiles ($I_N(x)$) of Nb clusters at 20 Kelvin with and without electric fields. Each vertical strip in the map is one deflection profile; the intensity is represented by pseudo color map, with red color for high intensity and blue for low intensity. In this case, all the $I_N^{V_d=0}(x)$ are normalized to be the same height(so that $I_N^{V_d=0}(0) = 1$), as shown in panel (a), and $I_N(x)$ with field is shown in panel (b). (c)(d)(e) Deflection profiles of three representative peaks, at size 19,37 and 38. Nb_{19} deflects as normal polarizable metal clusters, while Nb_{37} and Nb_{38} have wings in the deflection profiles. It is also obvious that Nb_{38} is more deflected than Nb_{37} as an example of the odd-even effect. (f) Electric dipole moments of Nb_N clusters measured at 20 K. For $N > 35$, all even-N clusters have larger dipole moments than the neighbor odd-N clusters

role in the dipole formations.

(2) Is it a dynamic effect or a bona fide low temperature effect? It was proposed [6] that the observed temperature dependence of the deflection behavior results from a dispersion in the rotational and translational speeds of clusters at different temperatures. At room temperature, the clusters are at higher speed (which scales as $\sim \sqrt{T}$), and the deflection (Eq. 4) is smaller than that at low temperatures, which reduces the dipole deflection. In addition, a faster rotation of clusters at high temperatures might also affect the electric deflection since there are still varying opinions regarding the deflection behavior of a dipole moment in an inhomogeneous field [40, 6, 7, 17, 16, 133, 54].

An important aspect of this thesis is to provide answers to the above questions. The experiments unambiguously demonstrate that the ferroelectricity in Nb clusters is really a low temperature effect and the origin of this ferroelectricity is caused by electron pairing interactions in clusters, which is further linked to the formation of Cooper pairs in clusters.

3.4 Photon Heating of Nb Clusters

It is possible to change the temperature of the clusters without significantly altering their dynamic properties. A straight forward way is to let the clusters absorb photons from a laser. The energy of an absorbed photon is enough to sufficiently heat the clusters. For a typical Nb clusters with 28 atoms, absorption of one photon (2.5 eV) is estimated to increase its temperature by 340 Kelvin, assuming that the heat capacity of an N-atom cluster is $3k_B$, where k_B is the Boltzmann constant. On the other hand, assuming the experiment is at 30 Kelvin, the relative change of the angular moment and momentum impacted by the photon is only 1/170 and 1/10000, respectively. Thus, the absorption of a photon will not significantly change the dynamics of the clusters.

In the laser heating experiments [50], a laser pulse is timed to hit the cluster beam right before it enters the electric deflection chamber. The energy per pulse is about 1 mJ at wavelength of 500 nm (2.5 eV), generated from an OPO laser (Continuum Panther). The linear response with laser fluence is check so that only 0 or 1 photon will be absorbed by a cluster during laser heating. The laser pulse is introduced from downstream of the cluster

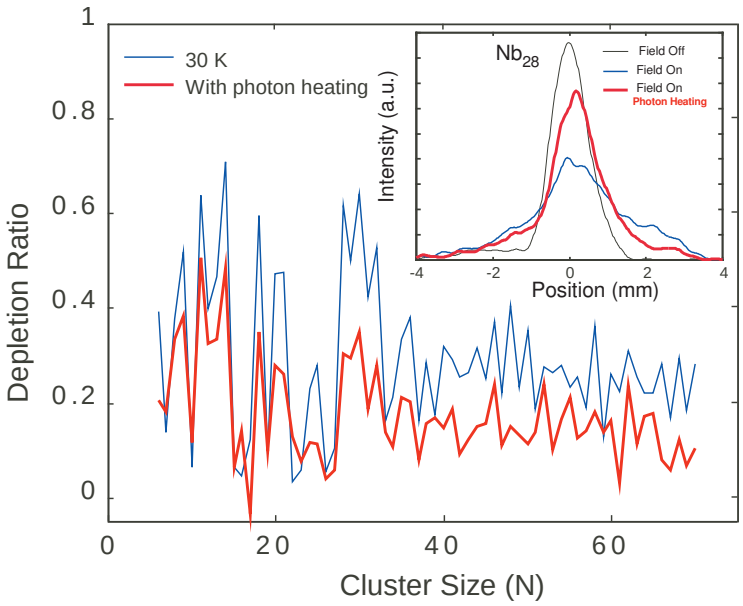

Figure 9: Comparison of height depletion of Nb clusters at 30 Kelvin without (thin blue line) and with (thick red line) laser heating. Some clusters absorb one photon and lose their dipole moments, resulting in reduction of height depletion. The power of heating laser pulse is about 1 mJ. (inset) Change of the deflection profile of Nb_{28} by laser heating. In the "field on" profile, some of the intensities at the wings are converted to the central peak after absorption of one photon.

beam and travels anti-parallel to the clusters beam. By carefully adjusting the timing of the laser, we ensure that it intercepts the cluster pulse at the point between the last collimation and the electric deflection plates (see Fig. 1).

We compared the electric deflection profiles of all clusters with and without laser heating, as shown in Fig. 9. Laser heating causes significant reduction in D_N for all cluster sizes. We find that $R_N = 1 - D_N(\text{laser on})/D_N(\text{laser off})$ increases approximately linearly with N, which should be interpreted as absorption ratio. If a single photon is sufficient to heat the cluster to above the transition temperature, then $R_N = F\sigma_N$, where F is the laser flux and σ_N is the absorption cross-section, which is approximately proportional to N.

Further analysis on deflection profiles reveals more information of the laser-heating effect. The deflection profiles are changed drastically by absorbing a photon, which is shown in the inset of Fig. 9 for a typical cluster of Nb_{28}. Some of the intensity from the wings

is converted to the central peak. We know that the wings represent clusters with permanent dipole moments, while the normal components are in the slightly-shifted central peak. Since absorption of a photon will not change the dynamics of deflection behavior, nor will it change the initial state distribution of the clusters (which is determined by the thermal equilibrium of clusters with the source), the only explanation has to be that laser heating has converted some of the ferroelectric clusters to normal clusters. In other words, there exist at least two types of clusters states; the clusters in the ground state have permanent dipole moments, while those in excited states have reduced or no dipole moment.

Note that the melting temperature of Nb bulk is $2477°C$, so the laser heated clusters are still well below the melting temperature. The fact that larger clusters (N up to 100) are also affected by photon absorption clearly demonstrated that structure change are not involved in the photon heating effect. For Nb_{100}, the temperature increase is only ~ 100 K, far below the bulk melting temperature.

These observations are consistent with our previous interpretations that the appearance of the dipole moment is a low temperature effect that appears when Nb clusters are in symmetry broken ground states. In any case, we have eliminated any explanations including dynamic effects.

3.5 Nb Alloy Clusters

To probe the nature of the ferroelectricity, we modify the electronic states of Nb_N clusters by introducing impurity atoms X (X = O, Al, Cr, Mn, Fe, Co, Ho, Au, Au_2 and Au_3). Impurity atoms with excess valence electrons will increase the number of electrons in conduction band of the clusters while those elements with large electron negativity such as F and O will absorb conduction electrons.

The impurity atoms are introduced by coating the Nb sample rod with desired element species. We limit our selection of impurity elements to those with only one or one dominant isotope because of resolution considerations.

Addition of one oxygen atom has some effects on D_N for $N < 25$ (Fig. 10B). In this size range, one oxygen atom slightly enhances the dipole moments; normal Nb_N clusters, such

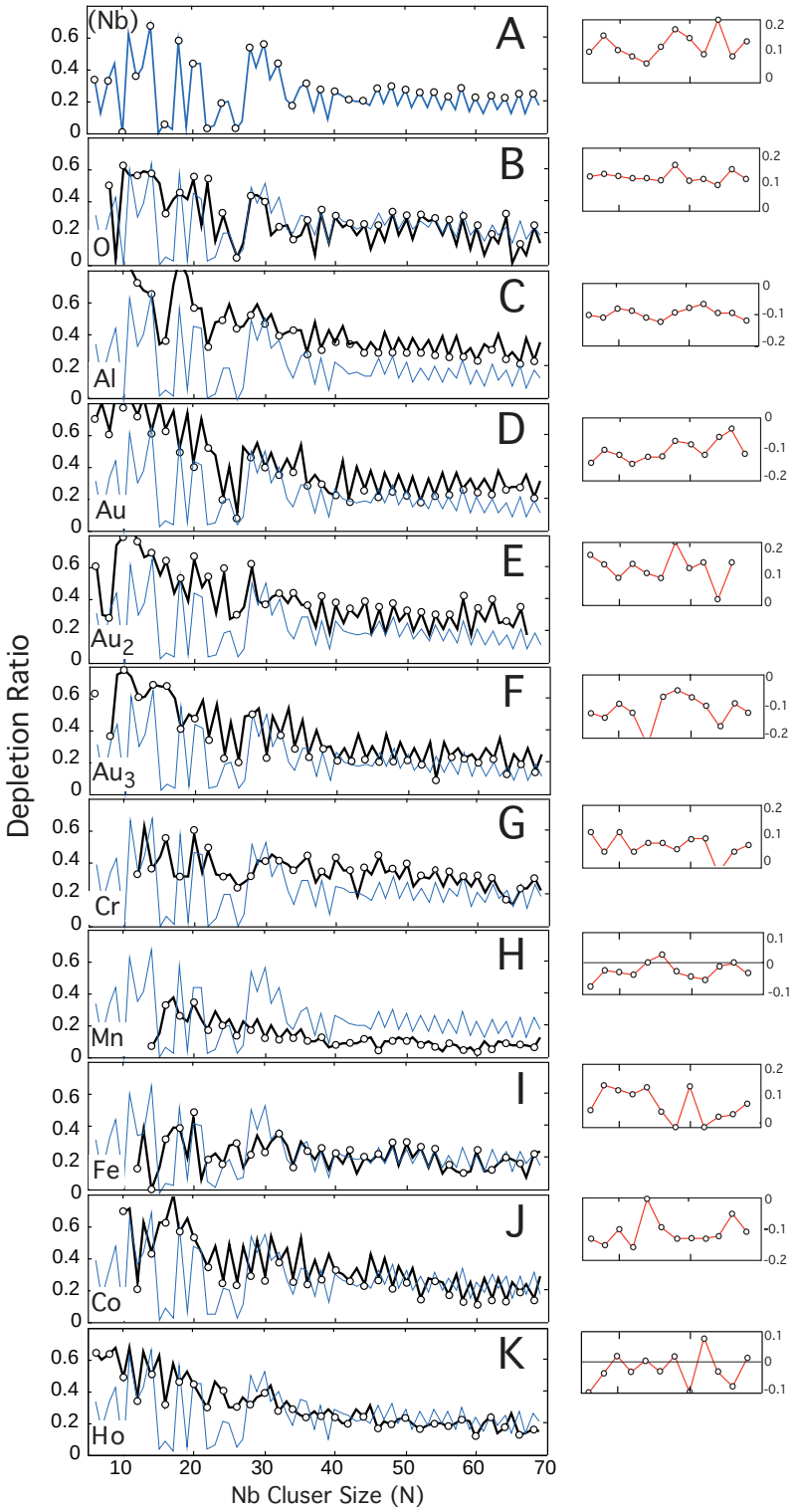

Figure 10: Depletion ratios of Nb_NX alloy clusters. The depletion ratios of the Nb_NX clusters (thick line) are compared with that Nb_N (thin line) measured in the same experiment. The panels on the right show the second differences of D_N for all even N in the range $45 < N < 70$. The even-N clusters are marked with open circles. All the experiments are performed at similar conditions at 20 K. The ferroelectricity shows dependence on total number of valence electrons. Al and Au impurities (C-F) enhance the ferroelectricity and magnetic impurities (G-K) depress it.

as Nb_{15}, Nb_{17} and Nb_{19}, acquire dipole moments with the addition of oxygen atoms. But for $N > 25$, D_N is barely changed and the same odd-even are observed in Nb_NO clusters as in Nb_N clusters, which is consistent with the oxidation of two electrons by an oxygen atom so that the total number of valence electrons is $n = 5N - 2$. Note that the oxidation will cause charge-transfer to the oxygen ion, but this seems to have little to do with the measured dipole moment, especially for larger clusters. This indicates that details of the ionic charge distribution is not playing the primary role on the formation of dipole moment in Nb clusters (compared with that in polar molecules such as HF and H_2O).

The addition of one aluminum atom causes large enhancements of the dipole moments (Fig. 10C). The normal Nb_N species are completely removed, and all Nb_NAl clusters show large D_N. For example, $D_N(Nb_{10}Al) = 0.94$, which is even close to saturation. The aluminum addition also inverts the odd-even dependence of D_N on N; all the Nb_NAl clusters with odd N now have larger dipole moments than even-N clusters. This is consistent with the fact that one Al atom has 3 valance electrons so that $n = 5N + 3$ and odd-N Nb_NAl clusters have even number of valence electrons, which favors pairing.

When Au atoms are doped in Nb_N clusters, the dipole moments are enhanced and we observe an extended odd-even alternation of D_N from $N = 6$ to 100 in Nb_NAu, but with opposite dependence on N (Fig. 10D). Au atom has a electronic structure of ($[Xe]4f^{14}5d^{10}6s^1$), when doped in Nb clusters, the extra 6s electron will be donated to the valence band and therefore, $n = 5N+1$, which is consistent with the inverted odd-even in Nb_NAu. This trend continues for Nb_NAu_2 and Nb_NAu_3 clusters: adding two gold atoms ($n = 5N + 2$) restores the odd-even, and adding three gold atoms ($n = 5N + 3$) inverts it again (Fig. 10E-F).

When impurity atoms with unfilled d or f shell are introduced in a metal host, they may produce a localized magnetic moment at the impurity site depending on local density of states and the strength of exchange interaction [9, 140, 53, 42, 56, 85, 135]. A 4f impurity in a transition metal host is expected to have local moment because of the strong localization of 4f orbitals. For 3d impurities, the condition for a local magnetic moment favors the nearly half filled elements. A magnetic impurity has a significant effect on electron pairing in superconductors, where the difference of the exchange interaction applied on spin-up and

spin-down electrons in a Cooper pair will weaken the pairing.

We are able to attach magnetic impurities of Cr, Mn, Fe, Co and Ho to pure Nb clusters (Fig. 10G-K). The magnetic impurities in general reduce the dipole moments and the reduce the amplitude of the odd-even effect. One Cr atom slightly enhances the dipole moment but reduces the odd-even of Nb_N. The residue odd-even effect is consistent with $n = 5N + 6$. Note that Cr, Mn, Fe and Co atoms have 6, 7, 8, and 9 valence electrons (4s and 3d), respectively.

Manganese has the largest effect on the dipole moments (Fig. 10H). Addition of one Mn atom almost extinguishes the dipole moment for $N > 40$; The remaining $D_N \sim 0.1$ is primarily due to peak broadening of the normal component. The odd-even effect is also greatly reduced in Nb_NMn. The weak odd-even alternation for $N < 40$ agrees with $n = 5N + 7$ for Nb_NMn.

An iron impurity also reduces D_N and the odd-even effect, but not as much as Mn (Fig. 10I). The odd-even dependence corresponds $n = 5N + 8$.

One cobalt atom suppresses both D_N and odd-even slightly for $N > 40$ (Fig. 10J). It appears to enhance the dipole moments for smaller clusters. The odd-even effect is line with $n = 5N + 9$.

One holmium impurity atom suppresses D_N at larger sizes ($N > 40$) and it enhances dipole moments for smaller sizes (Fig. 10K). The odd-even alternation seems to be greatly reduced by addition of one Ho atom; only small residue odd-even can be measured for $N < 20$, which favors larger D_N for odd N. Since 4f electrons of Ho atoms are deep from the Nb valance band, they should not be counted in the total number of valence electrons. Our observation suggests that one Ho impurity contributes odd number of valence electrons to Nb_N cluster, which is consistent with the typical +3 valence of Ho impurities in bulk compounds.

In order to quantify the change of dipole moments and odd-even effect upon alloying. We define $G_N = D_N(Nb_NX)/D_N(Nb_N)$ and $\Gamma_N = \Pi_N(Nb_NX)/\Pi_N(Nb_N)$, where the second difference $\Pi_N = D_N - (D_{N+1} + D_{N-1})/2$ is a measurement of the odd-even effect. [1] The

[1] It is similar to the parity gap defined to study superconducting grain [92].

Table 1: Alloying effect on the height ratio (G_N) and on the odd-even effect (Γ_N) of Nb_N clusters. Also see Fig. 10

Impurity	O	Al	Cr	Mn	Fe	Co	Ho	Au	Au_2	Au_3
G_N	0.76	2.42	1.41	0.43	0.95	1.08	0.90	1.91	1.60	1.67
Γ_N	1.44	0.95	0.59	0.22	0.65	0.98	0.19	1.07	1.23	1.11

average of G_N and Γ_N for various alloys for $45 < N < 75$ are listed in Table 1.

3.6 Ionization Potential

The ionization potentials IP_N of Nb_N clusters were measured for $2 \leq N \leq 120$, with a relative accuracy of about 3 meV. (Absolute uncertainties are larger; the measured values agree with Ref. [72, 142].) IP_N varies by only 0.12 eV in the range $N = 20 - 120$, and there is no distinct odd-even alternation.

The IPs can be compared with the semi-classical independent electron model for which IP_N = CC + WF + QSE. CC is the classical charging term, WF = 4.37 eV is the bulk work function, and QSE is the quantum size effect. CC = $\alpha e^2/(R_N + d)$ where R_N is the classical radius: $R_N = N^{1/3}R_1$, and d is the electronic spillout factor (from polarizability measurements [94], $d \sim 1.1$Å). We find that $\alpha = 0.2$, compared with the classical value $\alpha = 1/2$. This greatly reduced α value suggests an additional energy term proportional to e^2/R not included in the classical model. Following Kubo, QSE=E_F/n for odd-N clusters and QSE=0 for even-N clusters, so that in the range N=30-90, the IPs should present an odd-even alternation whose amplitude decreases from 0.040 eV to 0.014 eV. This is not observed. The IPs indicate that the energy level spacing at E_F is at least an order of magnitude smaller. These observations show that the usually successful semi-classical independent electron model fails quite dramatically for Nb clusters.

Further analysis reveals a residual QSE in the IPs of even-N clusters with their odd-N neighbors. This is brought to light in the second differences $Z_N = IP_N - (IP_{N-1} + IP_{N+1})/2$, by considering the cumulative sum over all even-N clusters $\sum_{\text{even}N} Z_N$. The overall rising trend in the range $N = 36 - 90$, corresponds to a slope of about 4 meV, which means the IPs for even-N clusters are in average 4 meV greater than their neighbor odd-N clusters.

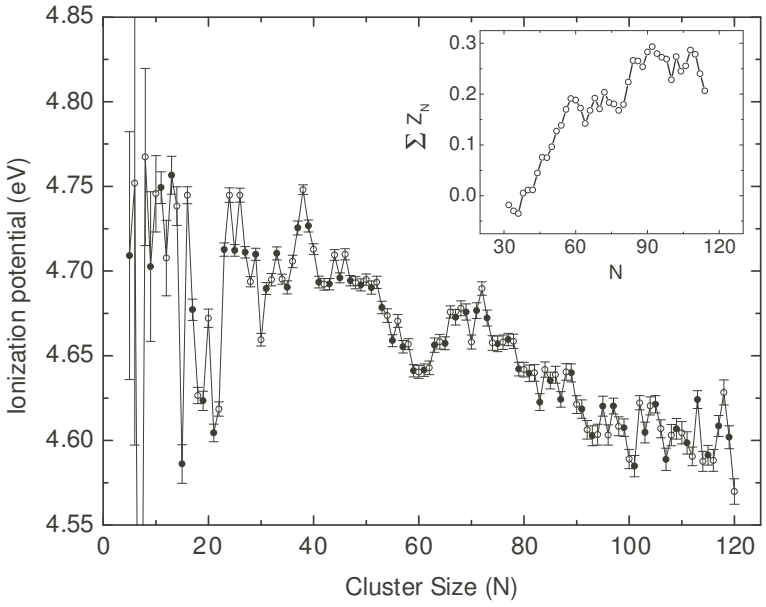

Figure 11: Ionization potentials of Nb_N clusters, which show no visible odd-even alternations, contradictory to the independent-electron model. (inset) The residual odd-even in IP_N are revealed in the cumulative sum of the second differences of IP_N for even-N clusters, which is determined to be about 4 meV.

This residual odd-even in the IPs is ten times smaller than predicted from the independent-electron model. Apparently the electron correlations that are neglected in independent-electron models have to be considered in order to give satisfactory explanations of the experimental observations.

3.7 Discussion

The ferroelectricity of Nb_N and Nb_NX clusters clearly demonstrates an odd-even dependence on total number of valence electrons. It shows a large response to single-electron attachment (in Nb_NAu), while it is not sensitive to ionic background perturbations (in Nb_NO). These facts all point to an electronic origin of the ferroelectricity in Nb clusters and their alloys

Furthermore, the experimental observations cannot be explained by the independent-electron model, which predicts a 10 times larger odd-even alternation in IPs than is measured. Such a model also fails to distinguish Nb clusters from other simple metal cluster that clearly do not show ferroelectricity. Apparently more subtle electronic effects have to

be taken into account for a satisfactory explanation.

The existence of permanent dipole implies large internal electric fields in Nb clusters, which, from electrostatic considerations, is estimated to $\sim 10^{11}$ V/m for a typical Nb cluster with 1 D dipole moment. This internal field clearly cannot exist in metals; the conduction electrons in metal will redistribute accordingly and screen out the field completely. Screening behavior is one of the basic properties that not only defines metals, but is also a property of metal clusters.

In the single-electron band picture, metallicity is defined as the absence of gap at Fermi level. But this definition does not apply well for clusters: when the size is reduced, the quantum size effect produce a Kubo-type gap ($\delta \sim E_F/n$) near Fermi level. Nevertheless screening can still exist in clusters; polarizability measurements and jellium calculations have shown that alkali clusters screen external fields well [21, 31]. Therefore alkali clusters should be categorized as "metallic" while HF and H_2O molecules are "insulating" [134].

From the screening behaviors in bulk and clusters, it is clear that screening is related to the delocalization of electrons in the system. If electrons are free to move, like in alkali clusters and bulk metals, they can redistribute easily to screen external field perturbations. (Our discussion here is limited to the response to long-wavelength static field, i.e., dielectric response $\epsilon(q, \omega)$ near $q = 0, \omega = 0$; there is subtlety of the screening near the Fermi wavelength $\sim 1/k_F$ [69].)

The localization of electrons in an insulator is a result of electron correlations. In molecules, the correlations causes the octet stability and the localization of electrons [60], which is responsible for the dipole moments in polar molecules such as HF and H_2O. On the other hand, in bulk, strong electron correlations can cause a metal-to-insulator transition (Mott insulators) [97]. [2]

Hence the loss of screening in Nb_N clusters clearly has its root in correlated electron motion. These correlations should arise from electron paring interactions, since they are sensitive if there are odd or even number of electrons (as shown above in the odd-even

[2]The single-electron type Bloch-Wilson metal-insulator-transition [139] is related to translational symmetry of the lattice, which is irrelevant to our discussion here for clusters.

effect). For odd-n clusters, the last unpaired electron is decoupled from the others and should still maintain full screening power as shown below. The depolarizing effect of the unpaired electron reduces the dipole moment, which explains the odd-even alternation of the dipole moment in Nb_N clusters (see below).

For a spherical even-N clusters of radius R_N and dipole moment P_N, the internal field produced in the cluster is $E_N = -\frac{P_N}{3\epsilon_0 v}$. The unpaired electron in odd-N will be polarized by this field and produce a dipole $P_s = \alpha_s E_N$ that opposes P_N. An estimate using a harmonic spherical potential shows that its polarizability is $\alpha_s = 4\pi\epsilon_0 r_s^3$, where r_s is the effective screening radius, and $(r_s/R_N)^3 \sim 0.35$ for $30 \leq N \leq 100$. Hence the odd-N clusters have $P_{N+1} = P_N + P_s = (1 - (r_s/r_N)^3) \sim 0.65 P_N$, which is consistent with our experimental observations (Fig. 8f). The large polarizability of a single electron also agrees with the good screening behavior of normal metal clusters, in which no electric dipoles have been observed.

The suppression of ferroelectricity in Nb cluster by magnetic impurities reveals another link between the pairing in Nb clusters and Cooper pairs in superconductors. It is well known that magnetism and superconductivity usually don't go together [91, 128, 2, 146, 23, 68, 82]. In superconductors, electrons that form Cooper pairs have opposite spins; while in magnetism, the spins are aligned. Accordingly Abrikosov and Gor'kov have shown that for magnetic impurities in superconductor, the exchange interaction between local impurity spin $\mathbf{S}$ and conduction electron spin $\mathbf{s}$ causes a reduction of T_c [2]. The exchange interaction with the local moment causes the splitting of the Fermi surface of spin-up and spin-down electrons. In other words, the magnetic impurities breaks the time-reversal symmetry in Cooper pairs and causes pair-breaking [146] [128].

The reduction of T_c is found to be linear with pair-breaking energy α

$$k_B(T_c - T_c^*) = \frac{\pi\alpha}{4} \tag{19}$$

where, T_c^* is the transition temperature with impurities. The superconductivity is completely destroyed for $2\alpha = 1.76 k_B T_c = \Delta_{BCS}$. Taking the form of exchange interaction to

Table 2: Suppression of T_c by 3d magnetic impurities in superconductors, from Ref. [52, 116, 148, 143].

Impurity	Superconducting Host	Suppression (K/%)
Cr	Nb, In, Sn	9.03 , 65, 16
Mn	Zn, Nb, In, Pb, MgB_2	295, 3.74, 51, 21, 159
Fe	In, Sn, Pb, $Mo_{0.8}Re_{0.2}$, W	2.25, 1.1, 4.7, 22, 15
Co	In, Sn, Pb	0.07, 0.15, 0.8

be $J(r)\mathbf{S}\cdot\mathbf{s}$, the pair-breaking energy is given by Abrikosov and Gor'kov [2, 128],

$$2\alpha \approx \frac{xJ^2}{E_F} \tag{20}$$

where x is the impurity concentration, J is average of $J(r)$ over atomic volume.

Experimentally for bulk Nb, a large reduction of T_c is observed for Mn doping [116], consistent with the large reduction of dipole moments and odd-even effects observed here. For other 3d magnetic impurities in superconductors, we compiled some of the available data in Table 3.7. The average T_c suppression by 3d impurities agrees with our observation that Mn has the largest effect on suppressing superconducting, while Co has the smallest among them.

STM experiments have been performed on Mn and Gd impurity atoms on superconducting Nb surface [146]. Those magnetic impurities are found to create localized electronic states in the superconducting gap and will eventually kill the superconductivity. The effect is larger for Mn impurities and smaller for Co and Fe impurities, which is consistent with our observations.

The enhancements of Nb_N ferroelectricity by Au and Al doping also have a counterpart in superconductivity. Among Nb alloys, Nb_3Al has one of the highest T_c (17.5 K); the T_c of Nb_3Au (11.3 K) is also 22% higher than pure Nb. Furthermore, as shown by Moro et al. [96], $Nb_{15}Al_M$ clusters have the largest D_N at $M = 5$, close to the 3:1 ratio where Nb/Al alloys have the highest T_c [124].

The similar responses of electron pairing in Nb_N and bulk superconducting Nb to magnetic impurities suggest a similar origin of the pairing interactions. We believe that a BCS-like paired ground state also exists in Nb clusters and there is a gap Δ_{NC} between the

ground state and the first excited states. In the IP measurement, the 4 meV IP difference should correspond to the breaking of a pair, giving $\Delta_{NC} = 2$ meV for $36 \leq N \leq 90$, which is close to Δ_{BCS} of the bulk (3 meV [120]).

On the other hand, the development of a dipole moment P_N in Nb_N costs extra Coulomb energy $P_N/2\alpha_N$. An estimate of the Coulomb energy gives 4 meV for Nb_{40} ($P_{40} = 1.5$ D), which is remarkably close to $2\Delta_{NC}$. In fact, we conjecture that the dipole energy should equal the paring energy $2\Delta_{NC}$. Since $\Delta_{NC} \to \Delta_{BCS}$ with increasing sizes, the dipole moment can be estimated to be $P_N \sim 0.25\sqrt{N}$ for large clusters, which reasonably agrees with the measurement (Fig. 8f).

We further discuss the possible origin of dipole moments by electron pairing. The formation of electric dipole requires breaking of inversion symmetry, which can be achieved by mixing of states of different parities. Consider two electronic states $|\psi>$ and $|\psi'>$ near Fermi level that are separated by $\delta = E_F/n$ and with different parities ($<\psi|ex|\psi'> = p \neq 0$). [3] Assuming two electrons in the states are subject to BCS type pairing interaction $H_{BCS} = -g\sum_{i,j} c^+_{i\uparrow}c^+_{i\downarrow}c_{j\downarrow}c_{j\uparrow}$ [92], we find the condensation energy to be

$$E_c = \sqrt{\delta^2 + g^2} - \delta, \tag{21}$$

which is larger for smaller δ. We argue that the condensation energy can be optimized by cluster deformations which will bring the two levels close together. In this case, with an electric field E applied, the ground state energy of the pair in the electric field is found to be,

$$E_g = -\frac{1}{2}(g + \sqrt{g^2 + 16p^2E^2}). \tag{22}$$

The polarizability of this pair is $\alpha_{Cooper} = -\partial^2 E_g/\partial E^2|_{E=0} = 8p^2/g$. Meanwhile, the polarizability of a classical metal sphere is $\alpha_{Cl} = 4\pi\epsilon_0 N R_N^3$ and when the system's polarizability is larger than α_{Cl}, the spontaneous formation of dipole moment is expected (known as the polarizability catastrophe) [61]. For the Nb_N clusters, we find $\rho = \alpha_{Cooper}/\alpha_{Cl} \sim 7 \gg 1$, so

[3] The two-level model is a simplification of the real Kubo single-electron levels in Nb clusters. The electrons near E_F are responsible for most electronic properties of the system. The polarizability for an electron in level $|i>$ is $2\sum_j \frac{|<i|ex|j>|^2}{E_j - E_i}$, so the contributions from electrons deep below E_F cancel each other and levels near E_F give the major contributions.

the Nb clusters can spontaneously acquire dipole moment in the ground state. It is worth noting that the polarizability catastrophe mechanism cannot produce a dipole moment in metals because of the screening; while in Nb clusters, the screening is reduced because of the formation of Cooper pairs (by creating a "crust" near Fermi surface that restrict motion of independent electrons). This mechanism only applies when the clusters are in their ground states. The thermally excited electrons are not in the paired states and will screen out the dipoles. This explains why like superconductivity, the ferroelectricity is only observed at low temperatures.

CHAPTER IV

FERROMAGNETIC ALLOY CLUSTERS

4.1 Introduction

4.1.1 Itinerant Magnetism

Magnetism is a result of quantum mechanics [132]. The magnetic moments of atoms come from two types of quantum motions of electrons: one is the orbital motion around nuclei; the other one is the electronic spin. The nuclei magnetic moments are several orders of magnitude smaller than that of electrons and contribute very little to magnetic moments of atoms.

When atoms assemble to form bulk material, atomic moments interact with each other to produce a variety of magnetically ordered structures. The bulk is ferromagnetic if all the atomic moments mutually align, and it is antiferromagnetic when the atomic moments from the sub-lattices cancel out each other [69]. More complex magnetic order can also be formed depending on the interactions between the atomic magnetic moments. Temperature is another important factor for magnetism in the bulk; at high enough temperatures, the regular magnetic order is destroyed and the bulk becomes paramagnetic [69].

Two physical models are used to describe magnetism in transition metals [69, 111]. In the Heisenberg model, it is assumed that the magnetic moments are caused by localized d electron spins. In this model, s electrons provide metallic bonding and d electrons provide magnetic moments. This localized picture is supported by observation of Curie-Weiss susceptibilities and spin waves in transition metals. But it cannot explain the saturation magnetization nor that the magnetic moments deduced from Curie-Weiss constant are larger than those determined from the saturation magnetization [48].

In the itinerant band model [111, 48], the magnetic carrier electrons are presumed to be itinerant, forming broad sp bands and narrow d bands. Because the localized feature of the d band, the exchange interaction will split it into spin-up and spin-down sub-bands. The

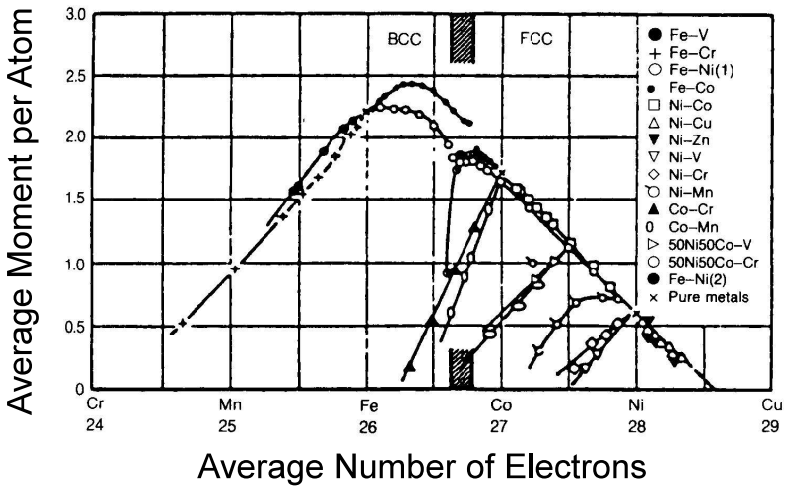

Figure 12: Slater-Pauling curve. Saturation magnetization (in units of Bohr magnetons) versus average number of electrons per atom. (After Chikazumi [24])

Fermi level is located in the middle of d bands. In this model, the imbalance between the spin-up and spin-down population is the origin of the ferromagnetism. The itinerant band model can successfully explain the fractional number of magnetic moments in transition metals but it gives poor description of their thermal properties [48].

4.1.2 Slater-Pauling Curve

Magnetic properties of alloys have been extensively studied since the 20's [102]. The most important property measured for these magnetic alloys is the saturation magnetization, which corresponds to the average magnetic moment (μ) at each atomic site.

The saturation magnetization of transition metal alloys plotted as a function of average number of valence electrons is called the Slater-Pauling plot [121, 107], which shows a regular and systematic behavior of saturation magnetization depending on alloy concentration. The most striking feature is the triangular shape, where most alloy species seems to follow the two equal and opposite slopes. On the right hand side are the Co and Ni based alloys such as Co-Ni, Ni-Cu, Ni-Zn, and Co rich Fe-Co alloys. These alloys all have the fcc or hcp structures. On the left part are the bcc Fe based alloys of Fe-V, Fe-Cr, and Fe rich Fe-Co alloys.

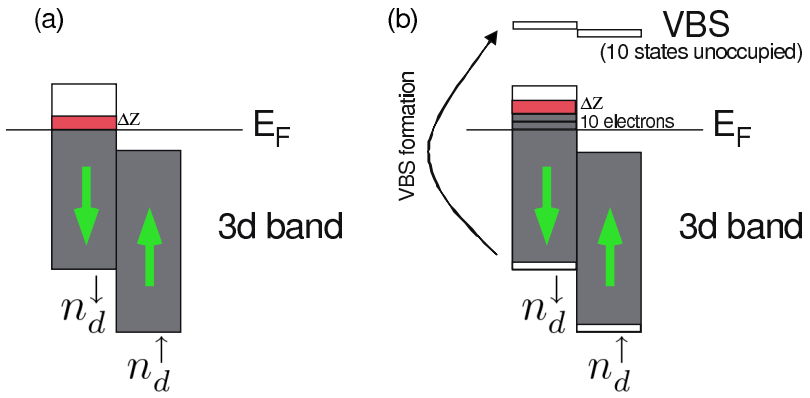

Figure 13: Illustration of the itinerant-band models of magnetism of transition metal alloys. (a) In rigid-band-model, the extra electrons ΔZ will fill up spin-down sub-band and reduce the total magnetic moment. (b) In virtual-bound-state model, localized states are created near the impurity atom. For early transition metal impurities, the VBS are above Fermi level; consequently, the spin imbalance is reduced by 10.

4.1.3 Rigid-Band Model

This triangular shape of the Slater-Pauling curve has been ascribed to itinerant electron magnetism from the very beginning [121, 107, 46]. These trends were first explained by Slater [121] and Pauling [107] using a simple rigid-band model. It is called rigid-band because it presumes that a small amount of doping will not change the band structure of the host and the electron deficiency or excess from impurities changes the filling (and the population imbalance) of the 3d band, which consequently changes the average magnetic moment. It is also assumed that the number of electrons in sp bands is not changed upon doping, therefore all the extra charges from solute atoms go to 3d bands. [1]

Let n_d,$n_d^{\uparrow}$ and $n_d^{\downarrow}$ be the average occupation of total, majority and minority 3d band respectively, there are:

$$n_d = n_d^{\uparrow} + n_d^{\downarrow} \tag{23}$$

The average magnetic moment (in units of μ_B) is determined by the imbalance between spin-up and spin-down population,

$$\mu = n_d^{\uparrow} - n_d^{\downarrow} \tag{24}$$

[1] The discussion below follows Williams and Malozemoff, et al. [87, 138].

Considering alloy $A_{1-x}B_x$ (solute B in host magnet A), the two elements have valence charges of Z_A and Z_B, and $\Delta Z = Z_B - Z_A$ is the charge difference.

Equations 23 and 24 can be re-written to be

$$\mu = 2n_d^{\uparrow} - n_d \tag{25}$$

Applying Eq. 25 on the host magnet, we get,

$$\mu_{host} = 2n_d^{\uparrow} - Z_A \tag{26}$$

If we assume that $n_d^{\uparrow}$ is constant on alloying. The extra $x\Delta Z$ electrons will further fill up the minority band and reduce the spin unbalance by $x\Delta Z$. Mathematically,

$$\mu = 2n_d^{\uparrow} - (1-x)Z_A - xZ_B \tag{27}$$

Combining Equation 26 and 27, the average saturation magnetization is

$$\mu = \mu_{host} - x\Delta Z \tag{28}$$

On the other hand, if we assume that $n_d^{\downarrow}$ is constant, then after repeating the same steps above, we get,

$$\mu = \mu_{host} + x\Delta Z \tag{29}$$

The change of sign in Equation 28 and 29 is the origin of the opposite slope on the two sides of the Slater-Pauling curve. On the right hand side, the alloys are strong magnets with the spin-up band fully occupied so that $n_d^{\uparrow} = 5$ is constant on alloying. As a result, Equation 28 applies, which describes the decreases of μ with increasing valence electrons. On the other hand, spin-down band in the bcc Fe host is split into two sub-bands, and the Fermi level sits in the band gap [87], which causes $n_d^{\downarrow}$ to be constant. That is the reason for the 45° slope for Fe based alloys on left hand side of the Slater-Pauling curve.

4.1.4 Virtual Bound States

While Eq. 28 and 29 explain the slopes of the Slater-Pauling curve, with the improved experimental and theoretical methods, it was later discovered that the bands are certainly not rigid at all. In the rigid-band model, the extra charge from solute will fill the host

3d band, which results in the transfer of the extra charge from the solute. But such large charge transfer contradicts Mossbauer and photoemission experiments [41].

As we have shown above, it is not actually necessary to assume rigidity of the band. The key points are the constancy of $n_d^{\uparrow}$ and $n_d^{\downarrow}$, which still could be valid even if the band is not rigid.

Friedel [46] first articulated an explanation that does not need to assume a rigid band. He realized that when an impurity atom with a different nuclear charge is doped into the metal, the metal system will not allow an internal electric field and the excess charge will be screened out. The screening comes from electrons near Fermi surface. For a strong magnet, the electrons have to come from spin-down band because the DOS of a spin-up band is zero at Fermi level. Therefore the spin-up occupation is not changed, which leads to Eq. 28. The same explanation also applies for Fe based alloys where the DOS of the spin-down band near the Fermi level is very small because it is in the gap, consistent with Eq. 29.

The screening of impurity charges involves the creation of virtual bound states (VBS) localized near impurity sites [46, 53, 9]. When impurity atoms are placed in metal, the energy levels of the impurity electrons will overlap with the host conduction band. The resonant scattering of the free electrons with the atomic levels will form localized virtual bound states. The states are virtual because they have limited lifetime and electrons only briefly populate them. The impurity atom are effectively characterized as deep potential well plus a centrifugal potential $l(l+1)/r^2$ (Fig. 14), VBS are the resonance states that formed in the potential well [53, 36, 131].

Another important result from Friedel is that when early transition metal atoms are doped into a later transition metal, the relative repulsive potential will push the VBS to above Fermi level. It turns out that the number of these states is exactly 10 for each solute atom. In this case, Eq. 28 is replaced by

$$\mu = \mu^{Host} - (\Delta Z + 10)x \tag{30}$$

Because $\Delta Z+10$ is always positive, this equation explains the "anomalies" in Slater-Pauling plot for branches of Co-Cr, Co-Mn, Ni-V, etc. (See Fig. 13 for the illustration of the models.)

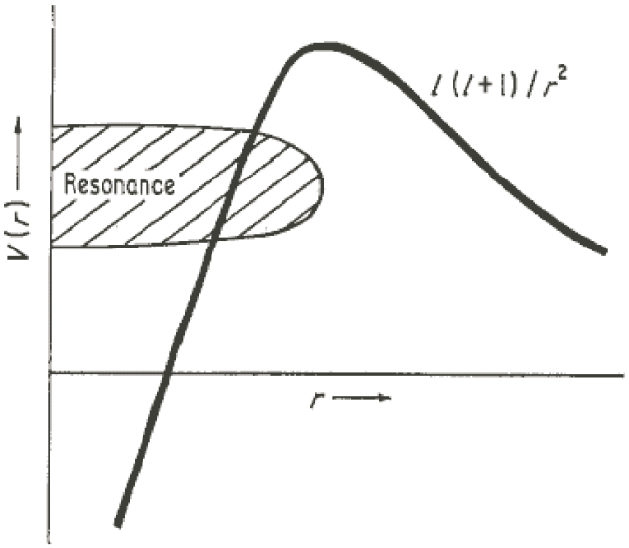

Figure 14: Schematic picture of virtual bound states near impurity site. The potential is a deep well near the center plus a centrifugal barrier of $l(l+1)/r^2$. This picture follows Gruner [53].

4.1.5 Magnetic Valence Model

Terakura and Kanamori [127] extended Friedel's picture to transition metal alloyed with a metalloid. The crucial question is whether the screening of metalloid sp electrons requires increasing N_{sp} by pulling more electron from d band near Fermi level to sp band. What they found is that the sp screening is actually caused by the polarization of 3d bands below Fermi level, without increasing average number of sp electrons. This polarization mechanism of the polarization is somehow similar to that in Friedel's picture [138].

To unify the above findings, Williams, Malozemoff, et al. [87, 138] proposed magnetic valence model, based on the constancy of n_{sp}. They introduced a magnetic valence for each element defined as

$$Z_m = 2n_d^{\uparrow} - Z \tag{31}$$

where Z is the valence and $n_d^{\uparrow}$ is the number of spin-up d electrons that one atom of the element will contribute when making alloys. The valence electrons include all the d and sp electrons.

$$Z = n_{sp} + n_d \tag{32}$$

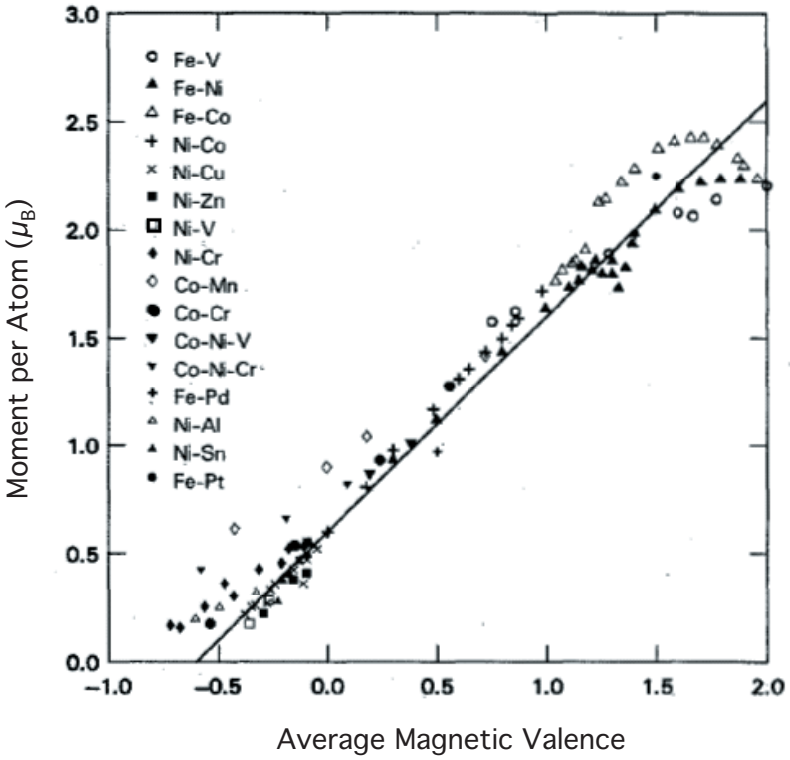

Figure 15: Generalized Slater-Pauling curve. Magnetization per atom is plotted versus average magnetic valence (After Williams et al. [138]). The 45° corresponds to a fixed number of sp electrons ($n_{sp} = 0.6$) in Eq. 33.

Note that the equations also hold if all the quantities are average values over all atoms instead of those from a single atom.

Eq. 31 and 32 can be used to eliminate $n_d^{\uparrow}$ and n_d in Eq. 25, which becomes

$$\mu = Z_m + n_{sp} \tag{33}$$

Given that in strong magnet the number of spin-up electrons for Fe, Co, Ni, Cu, ... Br and Kr atoms is 5, the magnetic valence for them is 2, 1, -1, 0, ..., -7 and -8, respectively. The caveat is that for early transition metals, the VBS are above the Fermi level and they are not populated. Therefore for the early transition metals $n_d^{\uparrow} = 0$ and $Z_m = -Z$. For example, the magnetic valence for Y, Ti, V, Cr and Mn is -3, -4, -5, -6 and -7, respectively.

With this new variable, all the transition metal alloys fall on a straight line defined by Eq. 33. The value for n_{sp} is found to be close to 0.6. Note that for Fe, Eq. 33 gives a value of 2.6 μ_B, which is larger than the measured saturation magnetization of Fe (2.2 μ_B). This

Table 3: Magnetic valence of some elements in the periodic table. These numbers are applicable only when the host is a strong ferromagnet of transition metals

Elements:											Al	Si	P
	Sc	Ti	V	Cr	Mn	Fe	Co	Ni	Cu	Zn	Ga	Ge	As
	Y	Zr	Nb	Mo	Tc	Ru	Rh	Pd	Ag	Cd	In	Sn	Sb
Z_m :	-3	-4	-5	-6	-7	2	1	0	-1	-2	-3	-4	-5

is because Fe is actually a weak magnet and spin-up band is not fully occupied.

4.2 Magnetic Alloy Clusters

As shown above, the ferromagnetism in transition metal alloys can be understood in itinerant band model. But whether this picture can be transfered to clusters is not know. To investigate alloy ferromagnetism in clusters, we performed accurate magnetic measurements on CoMn and CoV alloy clusters and compared them with the bulk counterparts in the Slater-Pauling curve. We also extended the work on Co clusters doped with metalloids in CoAl clusters. Finally, we studied the development of ferromagnetism in BiMn clusters where a small fraction of magnetic impurities (Mn atoms) is doped in non-magnetic host (Bi clusters).

4.2.1 CoMn and CoV Clusters

Here we present our magnetic measurements on Co_NMn_M and Co_NV_M clusters in the regime where less than 30% of Mn or V impurities are doped in Co clusters. We studied the change of magnetic moment as a function of doping for different cluster sizes.

Cobalt clusters are a perfect system to study cluster magnetism. Although it is the standard example of a strong itinerant magnet, yet the properties of cobalt clusters are still not fully understood [145, 144]. Alloys containing cobalt also constitute an important family of magnetic materials. Cobalt clusters are ideal for molecular-beam studies because Co atoms have only one isotope, making them perfect for high-resolution Stern-Gerlach experiments. In contrast, other iron group elements all have several isotopes which hampers the resolution. Mn is also an important magnetic element. It has a very high atomic magnetic moment of 5 μ_B. It is widely used as magnetic dopant in both molecular magnets and ferromagnetic semiconductors. However its function in alloy magnetism is still poorly

understood [70, 71, 147].

$Co_N Mn_M$ clusters have been produced and their photoionzation thresholds as well as their reactivities were studied in molecular beams [100, 78]. Experiments on their magnetic properties have not been reported to date. Likewise, to our knowledge, no magnetic studies of $Co_M V_M$ clusters has been reported.

The experimental methods are described in the previous chapters. The experiments are done at a temperature of 30 Kelvin and magnetic field of 0.99 T. These experiments have high accuracy (a few percent) to distinguish the magnetic moment differences of 1-2 μ_B on top of 40-100 μ_B. [2] The sample rods have diameter of about 2 mm and length of about 10 mm. Several types of sample rods were used in the experiments: $Co_{0.85}Mn_{0.15}$ and $Co_{0.5}Mn_{0.5}$ are purchased from Alfa Aesar; $Co_{0.88}V_{0.12}$ are produced in a home-made induction heating furnace. The magnetic moments are determined from deflections of cluster peaks in PSTOFMS.

Mn and Co atoms have atomic mass of 55 and 59 amu, respectively. The alloy peaks are separated by 4 amu, which is adequate for position-sensitive measurements. (Fig. 16).

4.2.1.1 Intensity Distribution

It is interesting to look at the intensities of $Co_N Mn_M$ and $Co_N V_M$ clusters that have the same total number of atoms. The probability to for a cluster with a certain number of Mn atoms follows binomial distribution (Eq. 10) where the average Mn concentration in clusters will be the same as that in the bulk sample.

The measured intensity I for a cluster can be expressed as [31]:

$$I = I_p C_t C_i C_d \tag{34}$$

where I_p is the intensity of clusters produced in the source, C_t is the source-to-ionization transfer efficiency, C_i is the ionization efficiency, and C_d is the detection efficiency. In this case, since we compare different cluster species of same size and small mass difference, C_t and C_d are expected to be about the same. The ionization potentials of $Co_N Mn_M$ clusters have

[2] For Co clusters, the average magnetic moment is about 2 μ_B per atom [18, 145].

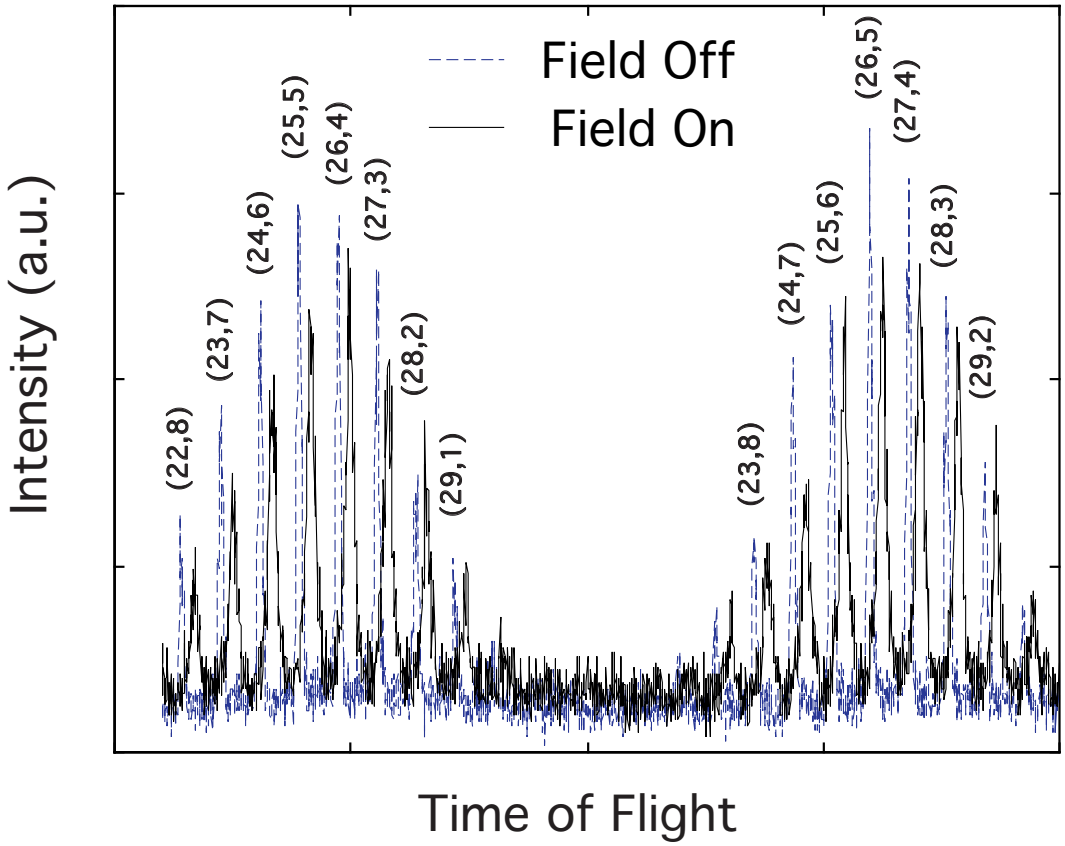

Figure 16: Part of the position-sensitive mass spectrum of Co_NMn_M clusters. Dashed line is the spectrum without magnetic field. Solid line is with a magnetic field ($B = 0.99$ T, $dB/dz = 30$ T/m) applied. The cluster peaks with field on are shifted to the right in time-of-flight as a result of deflections. From measuring the deflections of the corresponding cluster peaks, their magnetic moment can be determined. The Co_NMn_M species are unambiguously identified, which are denoted as (N, M) above the peaks.

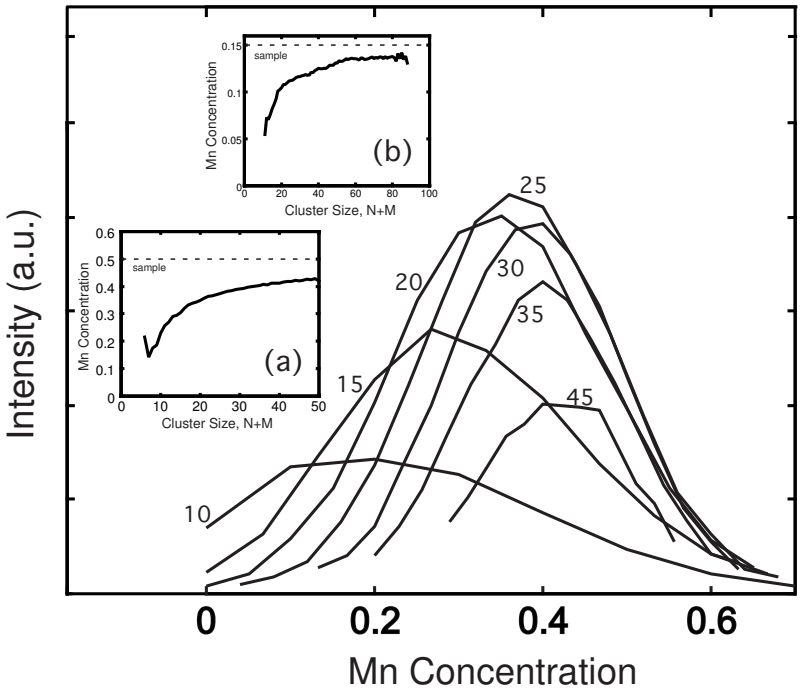

Figure 17: Mn concentration distribution of $Co_N Mn_M$ clusters for a $Co_{0.5}Mn_{0.5}$ sample. Each line corresponds to the measured intensity for a selected cluster size (fixed $N + M$), which is marked near the lines. The binomial distribution is clearly more Co-rich for small sizes. Inset (a) is the average Mn concentration by fitting the intensities using binomial distributions for all cluster sizes. Inset (b) shows the same fitted Mn concentration but for the $Co_{0.85}Mn_{0.15}$ sample.

been measured by Koretsky et al.[78], which show little dependence on Mn concentration for clusters at the same size. Therefore we expect C_i to be the same for $Co_N Mn_M$ clusters of the same $N + M$. Consequently, the measured intensity should be proportional to the intensity produced in the source.

While the V concentration in $Co_N V_M$ clusters follows binomial distribution very well, we find that the measured Mn concentration in $Co_N Mn_M$ clusters varies with cluster sizes. As shown in Fig. 17, the distribution is more Co-rich in small sizes and gradually approaches the bulk value in large sizes. We found similar behaviors for both $Co_{0.8}Mn_{0.2}$ and $Co_{0.5}Mn_{0.5}$ samples (Fig. 17 (a) and (b)).

It is known that production of $Co_N Mn_M$ clusters does not follow a statistical distribution. Sone et al. [123] are the first to point out that a $Co_N Mn_M$ cluster only can be produced with more than four cobalt atoms, based on their observation that there is a jump

at N=4 in mass spectrum of Co_NMn_M clusters. But more accurate experiments by Korestsky et al. [78] did not find the step at N=4. Instead, they found an enrichment at a small size range similar to our results (Fig. 17). But the trends have not been quantitatively studied or explained.

We explain the deviation of Mn concentration by considering the growth of clusters. From the measured intensity distribution at size N_0 (Fig. 18), one can predict the intensity distribution at size $N_0 + 1$ assuming that the probability to add one Co or Mn atom is proportional to its concentration in the sample. As shown in Fig. 18, it is obvious that the prediction matches measurement well for size larger than 8. Significant deviations from this prediction are found only for small sizes, where the measured intensity distributions are weighted toward the Co rich side (Fig. 18).

These deviations at small sizes mainly reflect the tendency to bind additional Co atoms instead of Mn atoms. On the other hand, at larger sizes, the clusters seem to bind both Co and Mn atoms equally. And the tendency to form Co-rich stable cluster at small size is the reason for the systematic deviation of Mn concentration in clusters.

Empirically the intensity distribution at $N_0 > 8$ can be reproduced very well by assuming that there is a critical size, N_c, below which only pure Co cluster can grow, and after N_c, Mn and Co atoms can bind equally during the growth procedure. The intensity distribution at size N_0 can thus be written as $p(N = N_0 - M, M) = \frac{(N_0-N_c)!}{(N_0-N_c)!M!}(1-x)^{N-N_c}x^M$. In fact $N_c = 7$ gives a reasonable fit to the intensity distribution for all sizes. This agrees very well our previous observation (Fig. 18).

From the intensity analysis of Co_NMn_M clusters, we conclude that Mn and Co atoms bind equally well in laser-ablation sources for sizes larger than 8 atoms. The formation of Co-rich clusters is favored at small sizes (less than 8 atom), which is consistent with previous observations [123, 78].

4.2.1.2 Magnetism of CoMn and CoV Clusters

The magnetic moments of all Co_NMn_M are determined from Gaussian fits to the deflection profiles. The total moments for Co_NMn_M clusters with different numbers of Mn atoms are

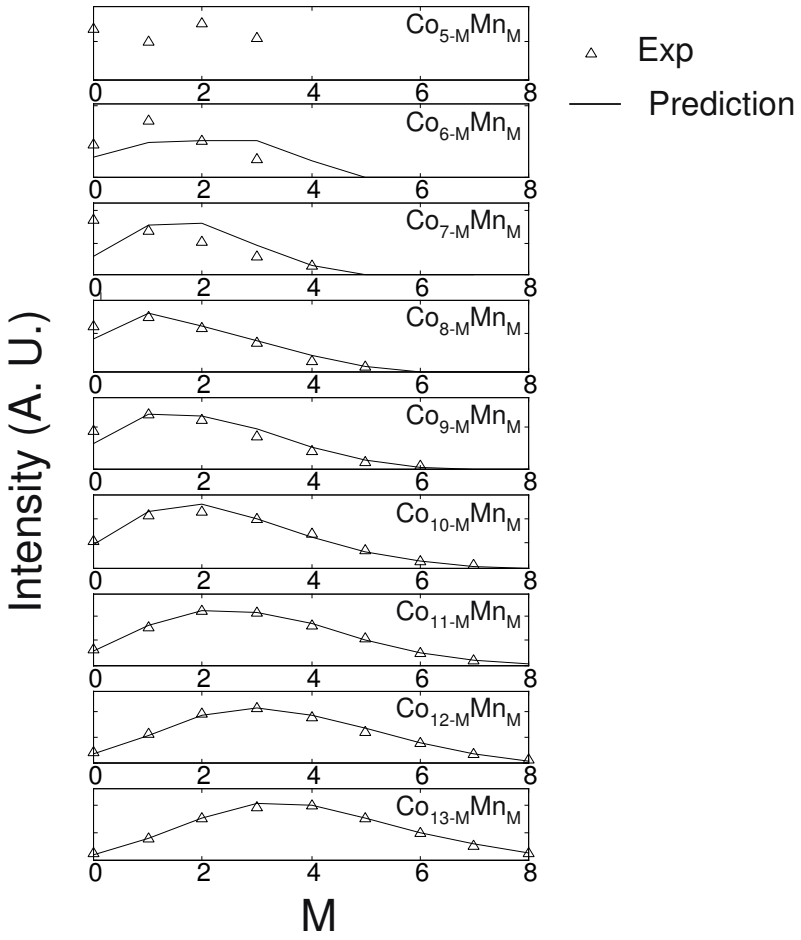

Figure 18: Growth model of Mn concentration in Co_NMn_M clusters. Each panel shows measured intensities of Co_NMn_M clusters of the same sizes (open triangle), which are compared with the predicted intensity distributions (solid line) based on the measurements on previous sizes. The predicted distributions fit the experimental measurements for large sizes ($N + M > 8$); the deviations are large for smaller sizes ($N + M < 8$) and towards Co rich clusters.

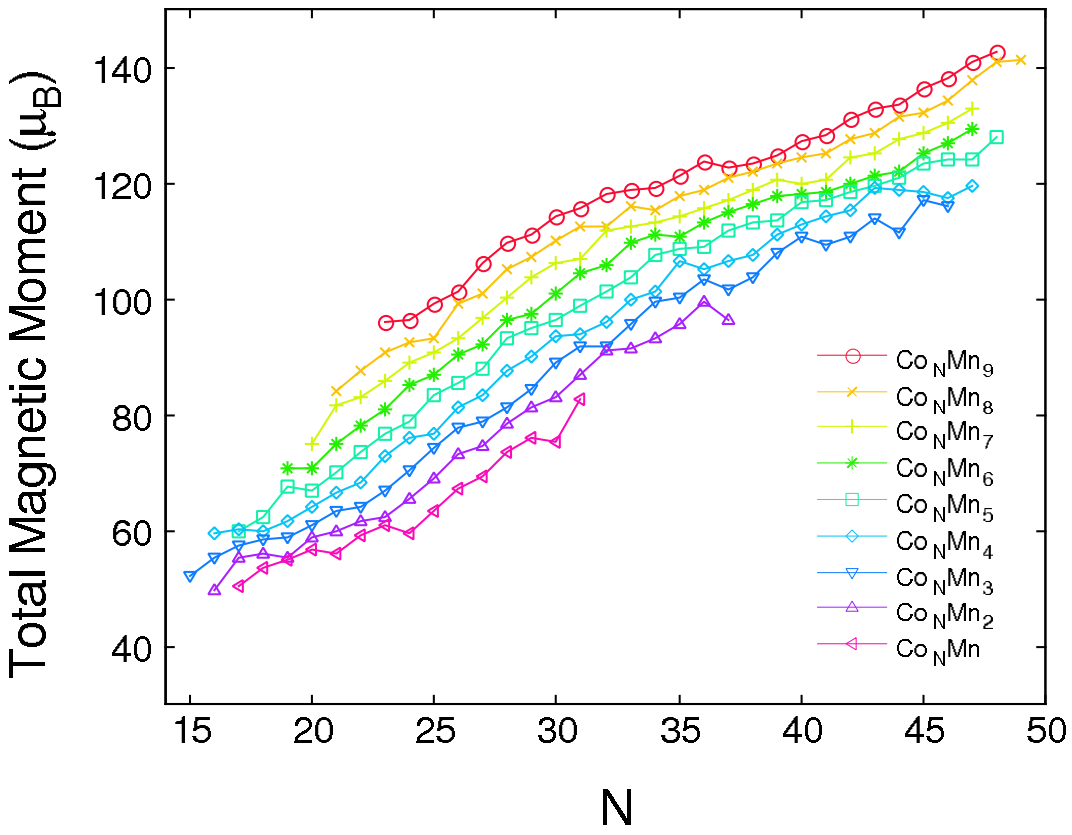

Figure 19: Total magnetic moments of Co_NMn_M clusters as a function of N. Each series represents clusters that have same number of Mn atoms. The measurement is performed at 30 K; the experimental uncertainty is around 1.5 μ_B

plotted as a function of the number of Co atoms in Fig. 19. The total moments can be seen to generally increase with the addition of Co or Mn atoms, indicating ferromagnetic contribution from both species.

It is more interesting to study the effect of Mn doping to eliminate the size dependence [18], which can be directly compared with the well known alloy magnetism in the Slater-Pauling curve. We keep the total number of atoms ($N_0 = N + M$) fixed and look at the average moment per atom ($\mu = \frac{\mu_0}{N+M}$) as a function of impurity concentration ($x = \frac{M}{N+M}$), which is plotted in Fig. 21(a) for some representative cluster sizes.

The first observation from the experimental results is that the magnetic moments of pure Co clusters are higher than that of Co bulk, which was attributed to the size effect, as has been observed by others [18]. We also find that the average moment increases linearly with

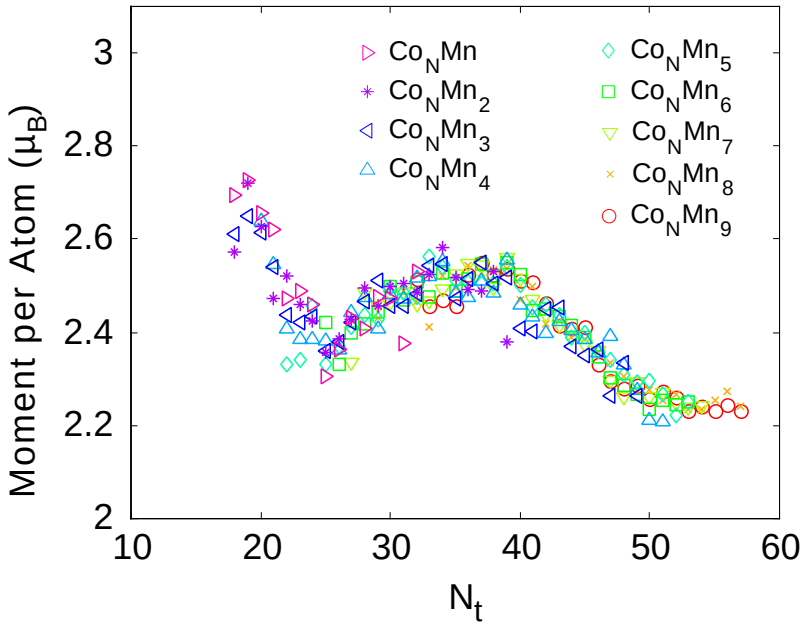

Figure 20: Average reduced moments for Co_NMn_M clusters. The extra contributions from Mn atoms (1.7 μ_B per atom) are subtracted. The average reduced moments show a dependence on total number of atoms.

Mn concentration. [3] The average enhancement by substitution of a Co with a Mn atom is determined to be $1.7 \pm 0.1\mu_B$ for all the alloy clusters in our experiments. Furthermore, the enhancement seems to be rather stable; it does not depend on the size or composition of Co_NMn_M clusters. This is shown in Fig. 20, where we plot the reduced moment per atoms versus size (total number of atoms). The reduced moment is obtained from the total moment by subtracting 1.7 μ_B for each Mn atom to account for the extra magnetic contribution. It clearly can be seen that now the reduced average moments overlap very well for all cluster species; the average reduced moments now depend only on the total number of atoms. [4]

The size dependence of a property usually gives valuable information about the origin of that property [62, 65]. For example, electronic shell structures have closed shells at 2, 8, 20, and 40. The observation of enhanced intensity at these sizes for alkali clusters is the result of the formation of the electronic shell structure. On the other hand, magic numbers

[3]The slope of the line (in unit of μ_B) is equivalent to the change of total moment by substituting one Co atom with one Mn atom, which plays a significant role in understanding magnetic contribution from impurity atoms.

[4]The size dependence is consistent with that of the magnetic moments of pure Co clusters [145].

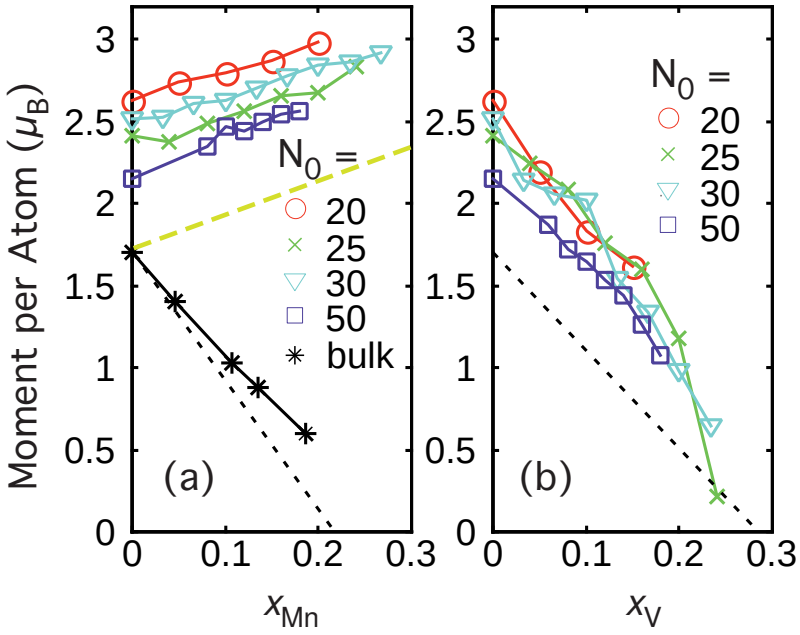

Figure 21: Magnetic moments per atom of (a)Co_NMn_M and (b)Co_NV_M clusters. Only several cluster sizes (N_0) are shown, other clusters have similar behaviors. The data for bulk CoMn (solid line) are from [30]. Dotted line is what expected for corresponding bulk if the VBS are completed above the Fermi level (Eq. 30). Each Mn atom substitution on average enhances the total moment by about $1.7\mu_B$, contradictory to the bulk behavior. On the other hand, the depression by V doping is consistent with the prediction for CoV bulk (6 μ_B)

observed at sizes 13, 19, 23, and 55 indicates icosahedral packing [70].

In the particular case of Co_NMn_M clusters, the size dependence on total number of atoms and constant enhancement by Mn all point to a collective picture. Recall that in the Slater-Pauling curve, the magnetic moments are determined only by the average number of valence electrons irrespective of the chemical composition. Our observations indicate a similar itinerant-band mechanism rather than geometric perturbations.

We also extended the measurements to larger Mn concentration regime by using a Mn-richer sample $Co_{0.5}Mn_{0.5}$. We find that the increasing trends persist only for Mn concentration up to 30% to 40%, after which the average moments start to drop with increasing Mn concentration. It can be expected that the average moment will finally approach the value of pure Mn clusters [70] with further increasing Mn doping.

The magnetic enhancement in Co_NMn_M can be contrasted to that of CoMn bulk, which is also shown in Fig. 21 for comparison. In bulk, the substitution of Co with Mn atoms

tends to decrease the average moment [30] by about 6.0 μ_B per substitution. These magnetic properties of CoMn bulk can be roughly understood by the VBS model discussed. For Mn impurities in Co, $\Delta Z = -2$, and the slope from Equation 30 is expected to be -8 μ_B. The results from CoMn bulk (-6 μ_B) are close to this expectation. The small difference can be explained by the fact that the nuclear charge different $\Delta Z = -2$ is not large enough to push the whole VBS above E_F. Band calculations has been performed for dilute Mn impurities in the Co hosts [125]. Mn local moments are found to have both anti-ferromagnetic and ferromagnetic coupling with Co with the anti-ferromagnetic state having lower energy. In both cases, the calculated average moments decrease with increasing Mn concentration.

The opposite slopes we observed in $Co_N Mn_M$ clusters is counter to our understanding of alloy magnetism; apparently the picture applied on bulk alloys needs to be modified for clusters.

Experiments on $Co_N V_M$ clusters shed some light on this issue. The average magnetic moments as a function of V concentration are plotted in Fig. 21(b). For $Co_N V_M$ clusters, in general the average moments decrease as the V concentration increases. The decreasing trends are similar for all clusters with only a few exceptions ($Co_{41}V_2$, $Co_{17}V_2$, $Co_{23}V_3$, $Co_{25}V_4$ and $Co_{19}V_6$).

There are no bulk CoV magnetization data available to compare. But calculations show that V in Co is the perfect case to form VBS well above the Fermi level [125], since the nuclear charge of V is 4 less than Co. Experimental data for Fe-V, Ni-V and CoNi-V alloys are in line with this picture [138] (See also Fig. 12). The predicted slope of -6 μ_B using Eq. 30 is completely consistent with our experimental results.

Note that these effects in $Co_N V_M$ cannot be explained by considering only Co moments. If V atoms are considered as magnetically inert additions to Co clusters, then the slope would have been $\sim$ -2 μ_B (i.e., the average contribution from a Co atom). The experimental observations in $Co_N V_m$ can be explained from an electronic-band point of view. The agreement between the measured slopes and that from Eq. 30 also proves that VBS exist in small clusters.

We further argue that the magnetic enhancement in $Co_N Mn_M$ is not caused by structural effects. The ionic radii of Mn and Co (in 12 coordinated metals) are very close, 1.26 Å and 1.25 Å respectively [69], and in bulk, up to 20% (59%) Mn can be dissolved into a hcp (fcc) Co solid without altering the host structure [59]. therefore, We expect the same behavior for Mn in Co clusters, i.e., small fraction of Mn atoms can be dissolved in Co without altering the structures.

The ground state geometry of Co clusters is not obvious. Bulk cobalt is either fcc or hcp and the average magnetic moment of fcc structured cobalt is only about 0.03 μ_B larger than that of hcp structure [63]. We expect that the structures of Co clusters to be either hcp, fcc or icosahedral based. Calculations show that the geometric structure of Co clusters has little effect on the total magnetic moments [114]. Furthermore, the magnetic-moment change caused by structural perturbations cannot explain the observed linear dependence on doping.

Indeed, our experiments suggest that the electronic bands (which determine the spin imbalance) are not altered by doping except in the creation of the VBS near impurity sites.[5] Each impurity atom substitution adds a constant contribution to the spin-imbalance according to its VBS and valence difference.

The magnetic enhancement in $Co_N Mn_M$ can be explained by assuming that the VBS is below E_F so that it is still occupied. In this case, Eq. 28 still applies and predicts a slope of 2 μ_B for Mn in Co, which is close to the measured 1.7 μ_B enhancement. The reason that the VBS is below E_F in $Co_N Mn_M$ clusters while it is above E_F in bulk alloy is not clear. We speculate that it is related to the details of the screening behavior in clusters, which itself is linked to the creation of VBS. This kind of unusual enhancement mechanism in clusters opens new possibilities of synthesizing high moment materials in the nanoscopic size and challenges magnetism theories.

Better understand can be obtained by further investigations on other alloy clusters species corresponding to the Slater-Pauling plot. It is not feasible in this work because of the existence of isotopes in other 3d elements. This difficulty can be overcome by using

[5] It is supported by the structure stability in $Co_N Mn_M$ clusters.

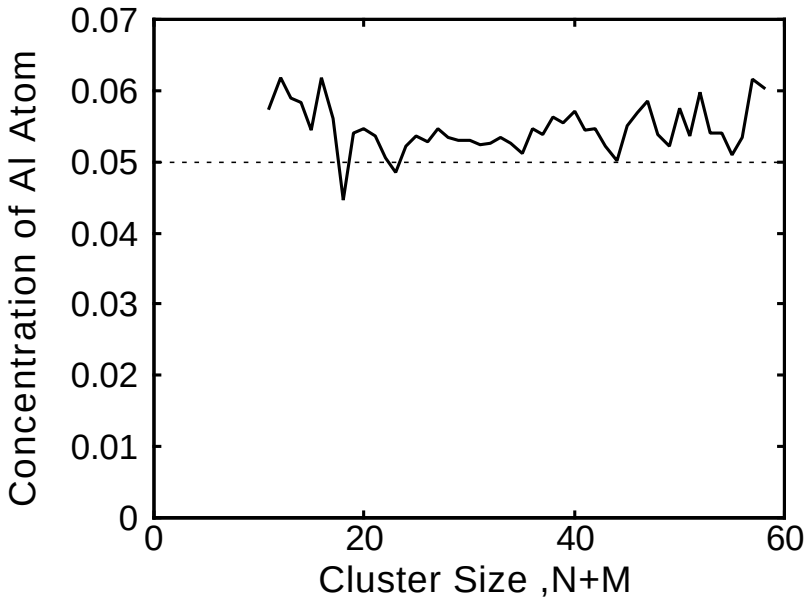

Figure 22: Al concentration for various cluster sizes. The concentration is from a binomial fitting of clusters intensities containing the same total number of atoms. The dashed line corresponds to the Al concentration of the sample rod (5%).

isotopically pure samples.

4.2.2 CoAl Clusters

We extended our work to Co clusters alloyed with Al atoms. Due to the low solubility of Al in Co bulk, we limited the concentration of Al to about 5% by using a $Co_{0.95}Al_{0.05}$ sample rod purchased from Alfa Aesar. This experiment was performed under the same conditions as the $Co_N Mn_M$ and $Co_N V_M$ experiments.

From the measurements we find very uniform Al concentration, as shown in Fig. 22. The Al concentrations in all cluster sizes are very close to 5%, as expected from the binomial distribution. The slight Al enrichment could come from the lower boiling point of Al than Co, which are $2519°C$ and $2927°C$ respectively.

The magnetic moments of the $Co_N Al_M$ clusters are measured from SG deflections. The per atom magnetic moments for several clusters sizes are plotted as a function of the fractional concentration of Al atoms in Fig. 23. The doping of Al atoms in general reduces the average magnetic moment. The depression is found to be related linearly with Al concentration. The average slope is about $-3.9 \pm 0.2 \mu_B$, which means every substitution of

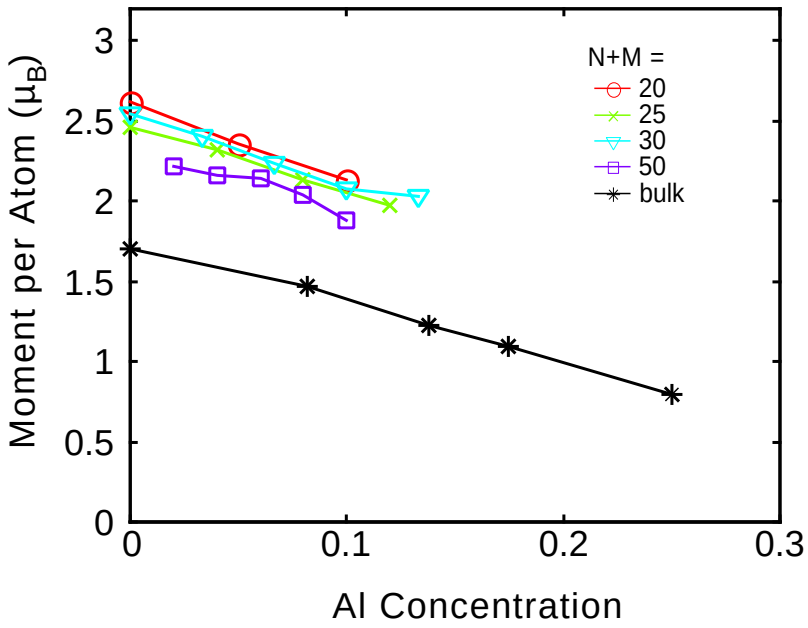

Figure 23: Average magnetic moment for some $Co_N Al_M$ cluster sizes. The clusters of other sizes have similar behavior. The CoAl bulk data is taken from Ref. [87]. Each Al doping reduced the magnetic moment by 1.9 μ_B, consistent with the behavior of CoAl bulk.

an Al atom with a Co atom will decrease the total magnetic moment of the clusters by 3.9 μ_B.

Clearly, this reduction cannot be explained by simply considering Al as magnetically inert additive. A similar electronic mechanism, as discussed in $Co_N Mn_M$ and $Co_N V_M$ clusters, must also play a role in $Co_N Al_M$ clusters.

In bulk, Al doping is found to linearly depress the average saturation magnetization of Co (Fig. 23). Williams et al. has explained this effect using the magnetic valence model. Z_m for Al and Co are -3 and +1 respectively; so every substitution of Co by Al will reduce Z_m by 4. From Eq. 33, this replacement will reduce the total magnetic moment by 4 μ_B, which is consistent with experimental observation in CoAl bulk. The prediction also gives excellent agreement with our $Co_N Al_M$ cluster data, where the average slope is around -3.9 μ_B.

In addition, we find that suppression of the magnetic moment by Al atoms is uniform and universal in $Co_N Al_M$ clusters. It seems to be independent of the size or composition. When we subtract 3.9 μ_B for each Al atom, the resulting average reduced magnetic moment

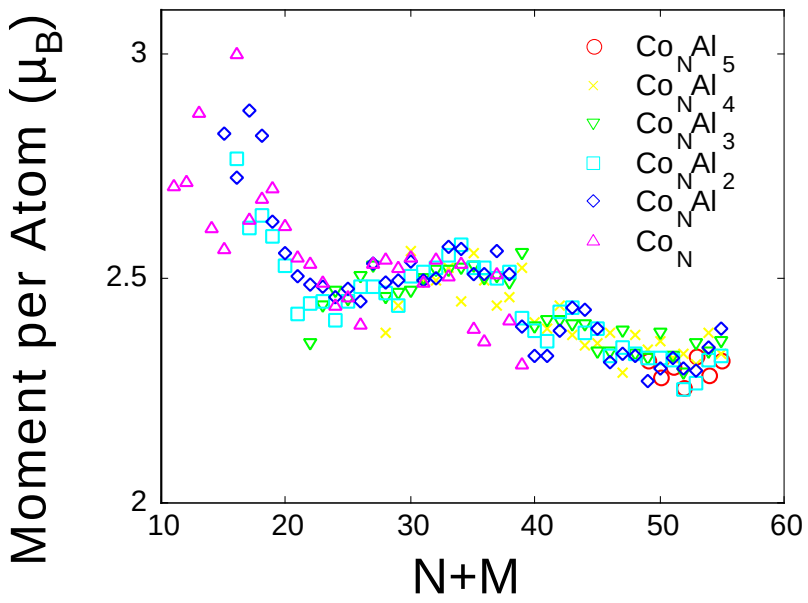

Figure 24: Reduced magnetic moment per atom for $Co_N Al_M$ clusters as a function of cluster size. Different symbols corresponds to the different number of Al atoms, which fall to the same line after -3.9 μ_B is subtracted for each Al atom. This reduced line corresponds to size dependence of magnetic moment for pure Co clusters [145].

as a function of size falls to one line, which corresponds to the average moment of pure Co clusters versus size [145].

In conclusion, the itinerant band picture seems to apply to the magnetism of $Co_N Al_M$ clusters. The extra p orbitals from Al atoms have not changed the number of electrons in sp band, which makes the generalized magnetic valence model capable of describing magnetic behaviors in $Co_N Al_M$ clusters.

It is not surprising that models developed for the bulk alloy apply fairly well to alloy clusters. After all, many properties of the bulk are similar to those found in clusters. Consequently we expect the converse to work as well: by studying magnetic alloy clusters, we can learn about alloy magnetism in the bulk. The search for new magnetic alloy materials can benefit from cluster studies because it is easier to perform experiments on a wide variety of composition and species in cluster beams than it is in the bulk.

4.2.3 BiMn Clusters

We next examine the development of ferromagnetism in clusters, where a small fraction of magnetic impurities are doped in non-magnetic host. The binary alloy cluster system

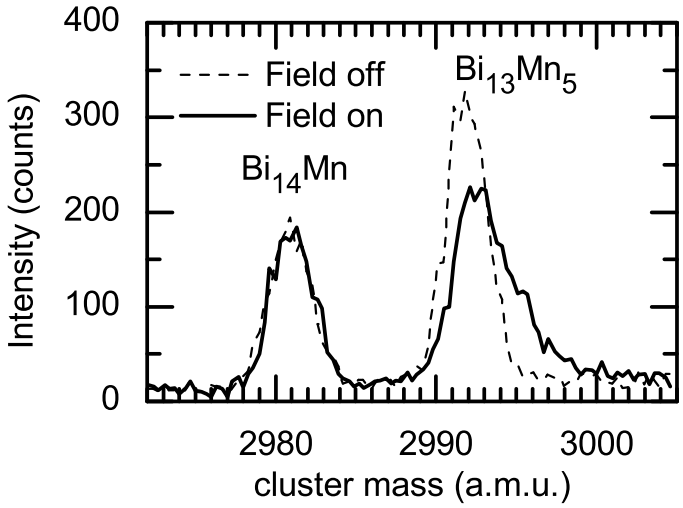

Figure 25: Position-sensitive time-of-flight spectrum of two adjacent peaks in the mass spectrum, $Bi_{14}Mn$ (2981 amu) and Bi_{13} Mn_5 (2992 amu). The thin dashed line is without magnetic field applied ($B = 0$), and the solid line is with $B = 0.91$ T. The shift in the mass peaks with the magnet on is due to the deflections. In this case, the $Bi_{14}Mn$ is shifted by 0.04 mm and $Bi_{13}Mn_5$ is shifted by 0.56 mm.

studied here, Bi_MMn_N,is inspired by the important properties of the bulk $Bi_{0.5}Mn_{0.5}$ alloy, known as bismanol, which is ferromagnetic with one of the largest known coercivities [3]. Manganese is an important magnetic element in molecular magnets and in ferromagnetic semiconductors [37, 64, 47, 103], which underscores the importance of this element as a component in novel magnetic materials.

The bismuth manganese alloy clusters are produced by laser ablation of a 2 mm-diameter rod of the alloy $Bi_{0.5}Mn_{0.5}$. The sample was prepared by co-melting Bi needles and Mn flakes in an electric arc furnace in an argon atmosphere using a home-built copper crucible with a cylindrical mold. The source temperature is maintained at $T = 46.5$ K the cluster beam is skimmed and collimated (to a width of about 0.3 mm) before entering the inhomogeneous magnetic field produced by the Stern-Gerlach magnet (B=0.91 T and dB/dz=345 T/m).

In the present case both manganese and bismuth have a single isotope and the cluster masses never coincide in the size range where we study them. Two typical position sensitive mass peaks are shown in Fig. 25. The masses are separated by 11 amu. When the magnetic

field is applied, the peaks are shifted toward the right side due to their spatial deflections.

Since the bismuth atom has an odd number of electrons, all Bi_N cluster with odd-N have at least one unpaired spin and hence they are paramagnetic. It is known that coupling of the spin to the rotations causes spin-relaxation-like effects, so that deflections are reduced and only toward high fields (which explains why earlier experiments on Bi clusters failed to detect deflections [150, 55]). The average beam deflection follows the Langevin equation even for very small cold clusters [145], as they do for warmer large clusters [66].

We see deflections in small odd-N clusters of pure Bi-N clusters (see Fig. 26). Odd-N clusters with N $\geq$ 5 show single-sided deflections, that is, they deflect uniquely in the direction of increasing field. Even-N clusters show no response. We further note that this result can be contrasted with the symmetric magnetic deflections that we observed in niobium clusters, which indicates that the spin is not coupled to the cluster in that case [95].

Figure 27 shows magnetic moment of Bi_N clusters as a function of N; the odd-even alternation is clear. The total magnetic moments of pure Bi clusters are less than 3 μ_B.

Adding manganese to these clusters generally enhances the magnetic response. The magnetic moments are presented in Fig. 28. Several clusters stand out with particularly large moments, for example Bi_5Mn_3, Bi_9Mn_4, $Bi_{10}Mn_5$, and $Bi_{12}Mn_6$. The data are graphically represented in Fig.29 which also shows the magnetic moments of pure manganese clusters [71].

Note in particular that the total magnetic moment is very sensitive to the number of Bi atoms in the cluster. For example the total magnetic moment of Bi_NMn_3 clusters varies from $3\mu_B$ to 11 μ_B in the range $2 < N < 20$. This can be contrasted with the Bi_NCo_M system [55], where not much size dependence was found for $M > 2$; and the magnetic moment is essentially exclusively determined by the value of M in that case. In this context, note that Bi/Co is an immiscible system so that a Bi_NCo_M cluster is probably segregated and hence the total magnetic moment is mainly due to the Co component. In contrast, Bi/Mn forms a compound, so that it is likely that Bi and Mn atoms are miscible in a Bi_NMn_M cluster. Note that the magnetic order of a Mn cluster is expected to be sensitive to its structure.

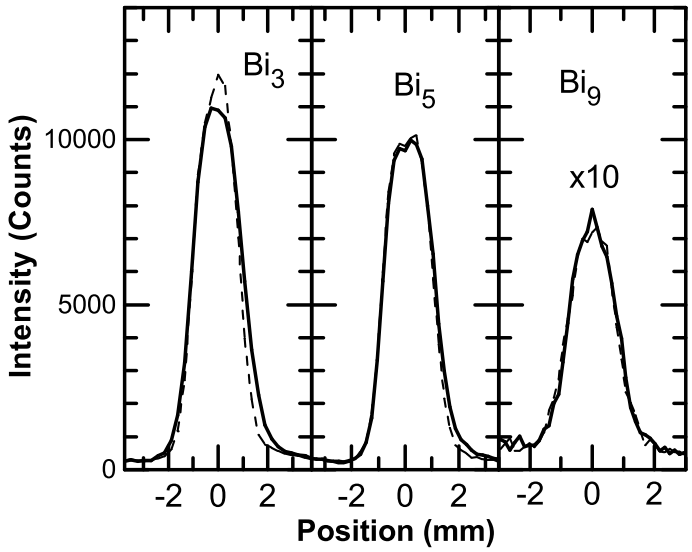

Figure 26: Deflection profiles of pure bismuth clusters Bi_N, N=3, 5 and 9. The thin dashed line is without magnetic field ($B = 0$), and the solid line is with $B = 0.91$ T. Notice that the trimer deflects both towards high field (the right in the figure) and lower field (left), but the pentamer deflection is single-sided. For the latter, the deflection is given by the Langevin equation.

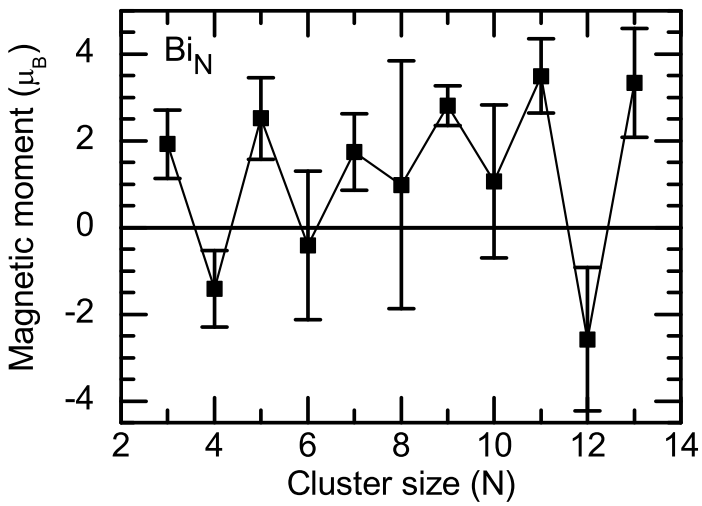

Figure 27: Magnetic moments of pure bismuth clusters determined from their magnetizations ($B = 0.91$ T, $T = 46.5$ K).

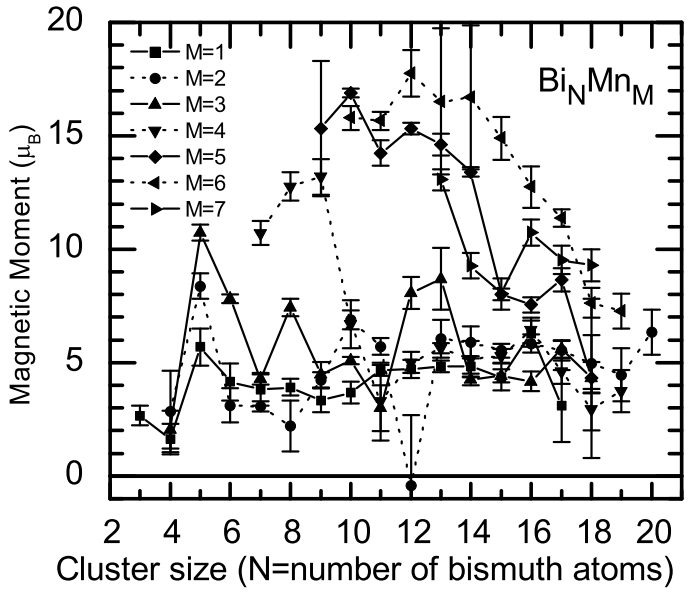

Figure 28: Magnetic moments of Bi_NMn_M. Note the particularly large moments of Bi_5Mn_3, Bi_9Mn_4, $Bi_{10}Mn_5$, and $Bi_{12}Mn_6$.

For example, Mn_N clusters are expected to be ferromagnetic for $N < 4$ and ferrimagnetic for $N > 5$ [98, 109] which is consistent with the experimental result for $N > 4$ [70]. Hence, one can speculate that the effect of the Bi in the alloy clusters is to modify the exchange interactions between the manganese atoms, which affects both the local moments on the atoms as well as the magnetic order.

A histogram of the magnetic moment per Mn atom for $M > 1$ (Fig. 30) sheds some light on the magnetic order. Two peaks are observed in the distribution: one is at $\sim$3 μ_B and the other around 1.3 μ_B. It can be argued that the clusters that show $\sim$3 μ_B per Mn atom are ferromagnetically ordered (all spins are mutually aligned) and the others have ferrimagnetic order (some of the spins are anti-aligned). The magnetic moment of $\sim$3 μ_B of a Mn atom in Bi_NMn_M clusters is considerably smaller than the 5 μ_B local moment suggested by Khanna et al.[67] for manganese clusters. This reduction can be understood as due to the Mn-Bi covalent interaction in these clusters [26]. For example, there are two phases for the manganese bismuth alloy: $Mn_{0.5}Bi_{0.5}$ and $Mn_{0.52}Bi_{0.48}$. Their saturation magnetizations per Mn atom are 3.8 and 3.1 μ_B respectively. The magnetic moment per

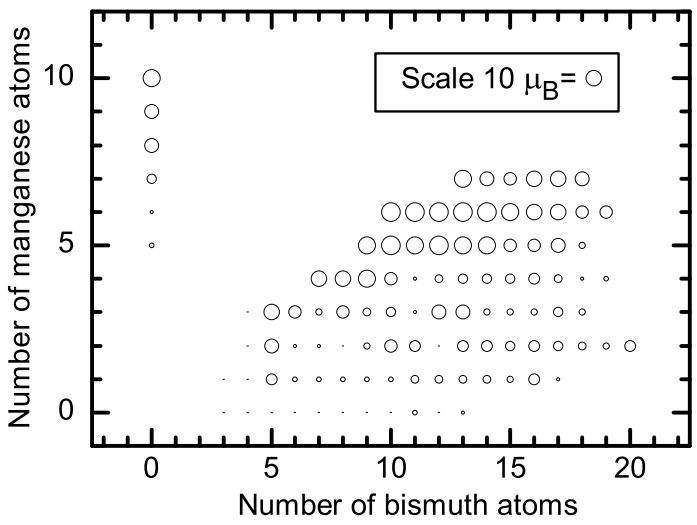

Figure 29: Magnetic moments of Bi_NMn_M as a function of N and M. The diameters of the circles are proportional to the total moments of the clusters. The data for pure manganese clusters are from [70].

Mn atom that we find in clusters is closer to that of the less symmetric phase $Mn_{0.52}Bi_{0.48}$.

Our data further indicate that ferromagnetic order usually occurs when Bi to Mn ratio is close to 2 (Bi_5Mn_2, Bi_5Mn_3, Bi_9Mn_4, Bi_10Mn_5 and Bi_12Mn_6), which suggests for this composition the separation between manganese atoms is optimal for ferromagnetic coupling.

In conclusion, low temperature Stern-Gerlach magnetic deflection experiments have been performed on Bi_NMn_M alloy clusters and pure Bi clusters. Pure Bi_N clusters are paramagnetic and exhibit an even-odd alternation; there is no evidence for ferromagnetism. Nevertheless, the magnetic moments of the alloy clusters are very sensitive to the number of Bi atoms in them: the maximum moments occur at approximately $N : M = 2 : 1$. This composition dependence suggests that the bismuth affects the coupling (and hence the magnetic order) of the manganese magnetic moments. The local magnetic moments of Mn atoms in these clusters are inferred to be about 3 μ_B. We surmise that the Bi atoms affect the magnetism in Bi_NMn_M clusters is two ways: (1) they bond with Mn atoms covalently and change their local magnetic moment; (2) they affect the inter-atomic distances between the Mn atoms which in turn affects the magnetic order.

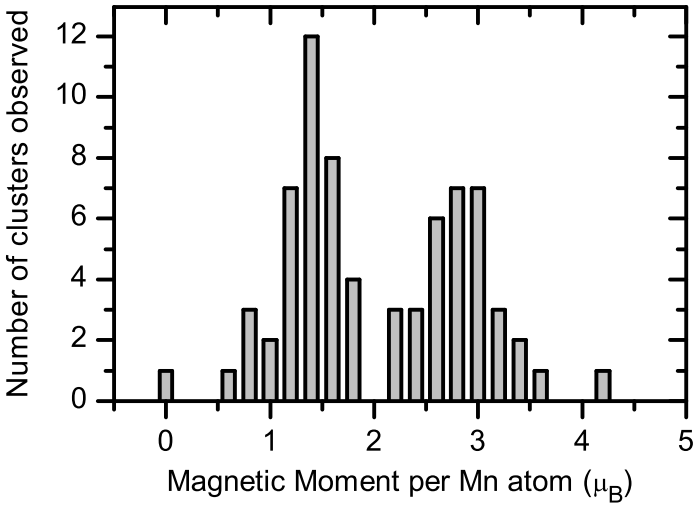

Figure 30: Histogram of the magnetic moments per Mn atom for Bi_NMn_M clusters observed in these experiments with more than two Mn atoms. The distribution is bimodal. The peak at 3 μ_B is identified with ferromagnetic coupling between Mn moments; the peak at 1.3 μ_B is identified with ferrimagnetic coupling.

CHAPTER V

CONCLUSION

From a wide range of molecular beam experiments, we showed that alloy clusters not only have intriguing properties themselves but also serve as powerful tools to study various properties in molecular beams.

From electric deflection measurements on Nb_NX (X = O, Al, Cr, Mn, Fe, Co, Ho, Au, Au_2, Au_3) alloy clusters, the electronic origin of the ferroelectricity in Nb clusters is unveiled, which further links to the existence of pairing interactions in these clusters. Formation of Cooper pairs in these clusters creates correlated ground states, which produce electric dipole moments as a result of reduced screening and mixing of electronic states of different parity. On the other hand, the unpaired electrons have full screening power and neutralize the dipole moments, which explains the odd-even effects and the absence of dipole moments in normal metal clusters. This pair formation is suppressed by magnetic impurities and thermal excitations, consistent with experimental observations. The explanation is supported by laser-heating and IP measurements on Nb_N clusters. The remarkable enhancement by Au and Au doping may lead to synthesis of strong correlated nano-materials at high temperatures.

Interesting magnetic properties are also observed in Co_NMn_M, Co_NV_M, Co_NAl_M and Bi_NMn_M clusters. Structural stability and the VBS model successfully explain the average moments' linear dependence on solute concentration, as well as their size-dependence on total number of atoms. The magnetism models developed for bulk apply very well in Co_NV_M and Co_NAl_M clusters and predict the depression by each V and Al substitution to be 6 and 4 μ_B, respectively, consistent with the measurements. The enhancement by Mn atoms, which is contradictory to the behavior in Slater-Pauling curve, is probably due to subtle modification of the screening behavior in clusters. This mechanism opens new possibilities of synthesizing high moment materials in the nanoscopic size and challenges

magnetism theories.

Moreover, we observed the development of ferromagnetism in Bi_NMn_M clusters. Mn moments are reduced by covalent bonding to Bi atoms; they also couple ferrimagnetically or ferromagnetically depending on the composition of the clusters. The maximum moments occur at approximately $N : M = 2 : 1$, where ferromagnetic coupling is favored.

APPENDIX A

TWO COMPONENT FITTING

In previous chapters we show that Nb clusters have two components. The clusters in ground states have permanent electric dipole moment; the clusters in excited states have no permanent dipole moment and deflect as polarizable clusters.

It is important to know the fraction of the two components and the magnitude of the dipole moment. The fraction of clusters in ground states at a given temperature gives valuable information about the energy gap between ground states and excited states. The magnitude of the dipole moment is related to the interplay of the condensate energy and electrostatic energy of the dipoles.

Experimentally, all the electric properties of clusters are measured from the deflection profiles of the cluster as it is deflected by inhomogeneous electric fields. What we obtained from deflection profiles are a mixture of deflections from both polarizable clusters and clusters with permanent dipole moments. Therefore, an efficient method is necessary to separate the two cluster components from the deflection profiles.

The method we use in this work is based on the different responses of these two components to various electric fields strength. A polarizable cluster is deflected uniformly toward the strong field direction; their deflection profile is ideally a purely shifted peak. The amount of the shift is proportional to the induced dipole moment of the clusters. In real situations, the electric field and gradient are not uniform across the beam and the deflected profile is slightly broadened.

The deflection of a cluster with a permanently dipole moment is still under debate [40, 6, 7]. But the generally accepted picture is that the cluster will change its motion adiabatically as it enters the electric field. In other words, the angular momenta, rather than the energy, are conserved when the field is turned on slowly.

In our experiment, we work in the low field limit, i.e., $P_0 E \ll k_B T$, where the deflection

profile of a permanent dipole fixed on axis in a spherical cluster can be written analytically as [16, 17]

$$I(x) = \begin{cases} \frac{1}{2x_0}\ln(\frac{x_0}{|x|}) & \text{for}(|x| \le x_0) \\ 0 & \text{for}(|x| > x_0) \end{cases} \tag{35}$$

where $I(x)$ is the probability to have a cluster deflected by a displacement of x, and x_0 is the maximum deflection of the dipole moment, which corresponds to deflection of the dipole moment if it always is aligned with the electric field. In addition, the permanent dipole is polarizable, which contributes extra shift of the deflection profile.

In experiments, we can apply as much as 80 kV/cm deflecting electric field, which is limited by the discharges between the electric plates. For Nb_{28}, the typical induced dipole by electric field of 80 kV/cm is about 0.04 D, while its permanent dipole is ∼2.6 D. The deflection caused by polarizability is about a hundred times smaller than that caused by permanent dipole moment even with the largest electric field in our experiments.

But the large deflections by a permanent dipole is still not sufficient to separate the two components. Because in the logarithmic distribution (Eq. 35), the most of intensity is not deflected, and only very small amount can extend to the maximum deflection. Even at the largest field and lowest temperature, we still cannot fully separate the two components. In addition, our apparatus only allows position-sensitive detection within a 4 cm effective window, which is limited by the width of the expanded excimer laser beam. This constraint limits our ability to deduce reliable information by fitting the tails of the deflection profiles.

The method we use in this work focuses on the relative height change of the deflection profiles as a function of the electric field. Since the height of the deflection profile of a permanent dipole decreases with the increasing field while that of a polarizable cluster ideally does not, it is possible to separate the two components from their field dependent behaviors. In addition, the maximum height of the deflection profile is always within the detector window, which allows larger electric fields to be applied for better separation, even though the tail will extend beyond the detection window.

Let the fraction of polarizable cluster be a, and the fraction with permanent dipole is $1 - a$; then given the measured height changes at various electric fields, the method seeks

the best fit of a and P_0. For simplicity, we also assume that the two components have the same polarizability, because the data are not enough to fit three parameters accurately.

The field dependence of the deflection profile in Eq. 35 is in x_0, which is calculated as

$$x_0 = P_0 \frac{l(L + \frac{l}{2})}{mv^2} \frac{dE}{dz} \tag{36}$$

where l is length of the electric deflection plates, L is the distance from the center of deflection plates to the detector, E and dE/dz are the electric field and field gradient in horizontal direction, and m and v are the mass and speed of the cluster. It can be simplified as $x_0 = kP_0V$, where k is the geometric factor that is fixed in the experiments and V is the high voltage applied to produce the electric field.

In practice, the width of the cluster beam has to be considered, and the measured deflection profile is a convolution of the theoretical deflection profile and the undeflected beam profile (without electric field). Assuming the beam has finite width σ, the undeflected profile can be approximately described as a Gaussian function $f(x)$,

$$f(x) = \exp\left(-\frac{x^2}{2\sigma^2}\right) \tag{37}$$

With the applied field, the measured deflection profiles $g(x)$ can be expressed from a convolution of $f(x)$,

$$g(x) = [a\delta(x - x_p) + (1 - a)I(x - x_p)] \otimes f(x) \tag{38}$$

where x_p is pure shift caused by the polarizability.

Then, the maximum value of $g(x)$ is compared with that of $f(x)$ to get the peak height ratio as a function of the applied voltage. Note that the maximum values of $f(x)$ and $g(x)$ are at $x = 0$ and $x = x_p$, respectively.

$$r(V) = g(x_p)/f(0) = [\alpha\delta(x) + (1 - \alpha)I(x)] \otimes f(x) \tag{39}$$

From Eq. 37 and 38, $r(V)$ can be calculated:

$$r(V) = a + (1 - a)h(t_0) \tag{40}$$

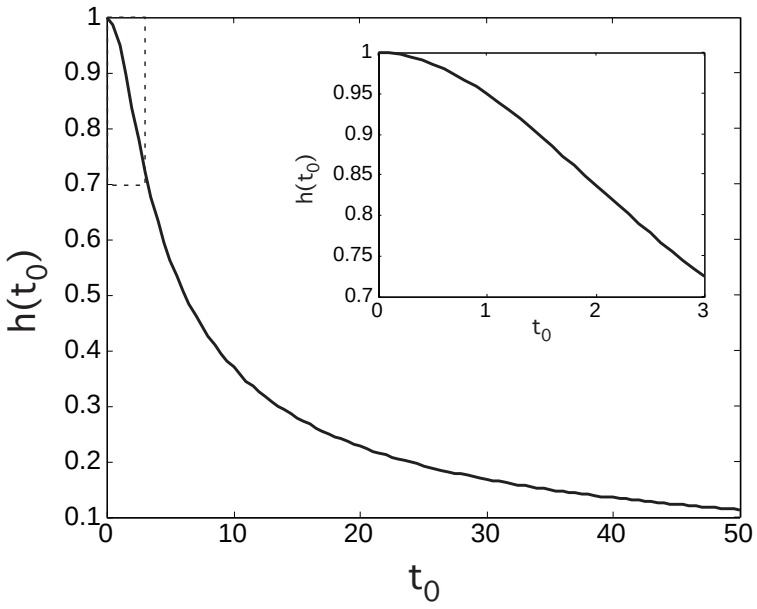

Figure 31: Height ratio (h) of the dipole deflection profile as a function of t_0. $t_0 = kP_0V/\sigma$ is the maximum deflection of the dipole moment in units of cluster beam widths. $h(t_0) \sim 1/t_0$ when $t_0 \gg 1$, and $h(t_0) \sim 0$ when $t_0 \ll 1$. The inset shows enlarged range of $0 < t_0 < 3$.

where t and t_0 are the deflection and the maximum deflection calculated in units of beam widths (σ), $t_0 = kP_0V/\sigma$, and

$$h(t_0) = \int_{-t_0}^{t_0} \frac{1}{2t_0} \ln(\frac{t_0}{t}) \exp(-\frac{t^2}{2}) dt \tag{41}$$

is a universal function of t_0 that corresponds to the reduction of peak height by the dipole deflection. The universal curve of $h(t_0)$ is shown in Fig. 31.

Since t_0 scales as $\frac{P_0V}{\sigma mv^2}$, in order to have the best resolution of the height change, it is desirable to have high field, low speed, and narrow cluster beams. Larger clusters also tend to have smaller height changes. In the extreme case of $t_0 \ll 1$, $h(t_0) \sim 1$, which is easy to understand because it corresponds to very small dipole deflection compared to the beam width, so the height of the profile is not affected by the deflection. On the other hand, when $t_0 \gg 1$, $h(t_0) \sim \frac{1}{t_0}$, which corresponds to much larger deflections compared with the beam width. In the calculations, we generated a lookup table by numerically integrating Eq. 41 in the range $0 \leq t_0 \leq 1000$. The lookup table has more data points at small t_0 to describe correctly the shape of the $h(t_0)$ curve. During fitting, the value of $h(t_0)$ is obtained by linear interpolation of the lookup table at any given t_0 value.

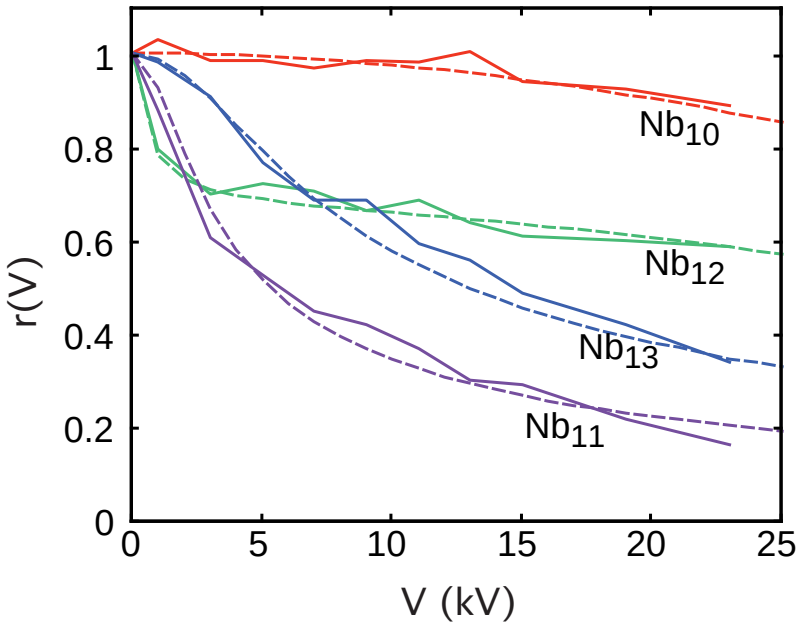

Figure 32: Two component fitting of the height ratio for several Nb clusters. Solid lines represent measured $r(V)$. Dashed lines are the $r(V)$ from the two component model. Note that $r(V)$ have very different behaviors for different clusters. For example, it drops very fast for Nb_{12} at low field then reaches a high value; while $r(V)$ for Nb_{11} decrease slower at low field but approach much lower value. The different behaviors cannot be fitted with models with only one dipole component; at least two components are necessary to have good fit.

Experimental data $r(V)$ are measured and fitted using Eq. 40 with two parameters, P_0 and a, until the RMS difference is minimized. This method is similar to the one that Dugourd et al. used to find dipole moment of $Co_{60}Ti$[40], except that we have additional parameters for normal component. Since the deflection is inversely proportional to mass, the accuracy of the fitting is better for small clusters. and we have larger uncertainty for larger sizes.

We also consider the broadening of a purely deflected peak. The widths of all the clusters in an experiment are the same so the broadening is determined only by the amount of pure deflection. Since we already know that some Nb clusters, such as Nb_{10}, Nb_{15}, Nb_{17}, etc., only have pure deflection, so based on the measurement from these clusters, we can construct empirically a height change versus deflection relation, which is a quadratic function of V.

The energy scale of the gap between ground states and excited states is deduced from

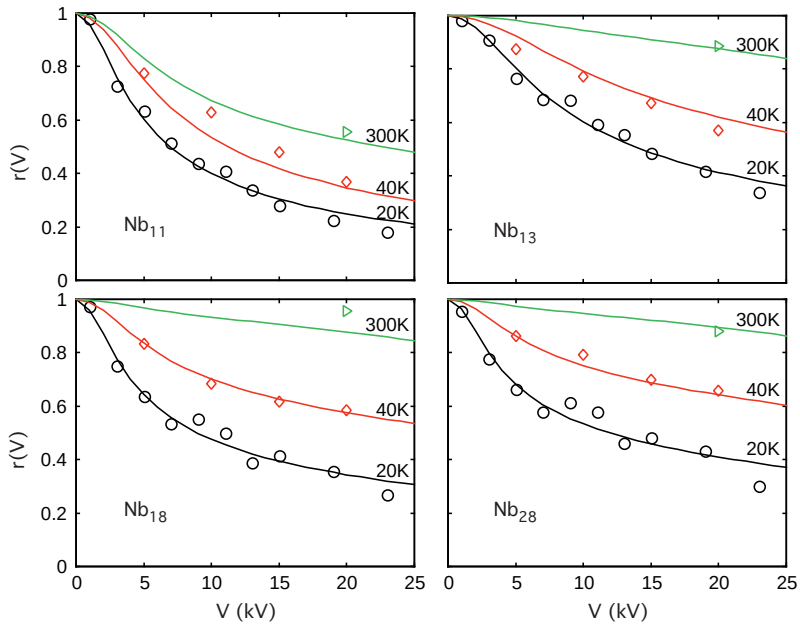

Figure 33: Comparison of two-component fitting at various temperatures. The dipole moments and transition temperatures are obtained from 20 K data, and the expected $r(V)$ at higher temperatures (40 K and 300 K) are compared with experimental data. The fit is reasonably good for most cluster sizes.

the components measured at certain temperatures. We do not know the exact energy level distributions of the two components, but the simplest estimate is to assume that the energy levels are uniformly distributed and the clusters at states below a certain energy $k_B T_g$ have dipole moment, and T_g is ferroelectric transition temperature. The uniform distribution of states gives the relation between T_g and the a,

$$T_g = -\ln(a)T. \tag{42}$$

Note that the fitting is done only at low temperature (20 K). When we use these parameters on high temperature data, they also fit except for a few small clusters Nb_6, Nb_8 and Nb_{12} (Fig. 33). Therefore, we can concluded that all of above assumptions work reasonably well for most clusters. Note that Eq. 42 can be also written as $a = \exp(-T/T_g)$, which is similar to the excitations in a superconductor which has a gap $\Delta_{BCS} = 1.76 k_B T$.

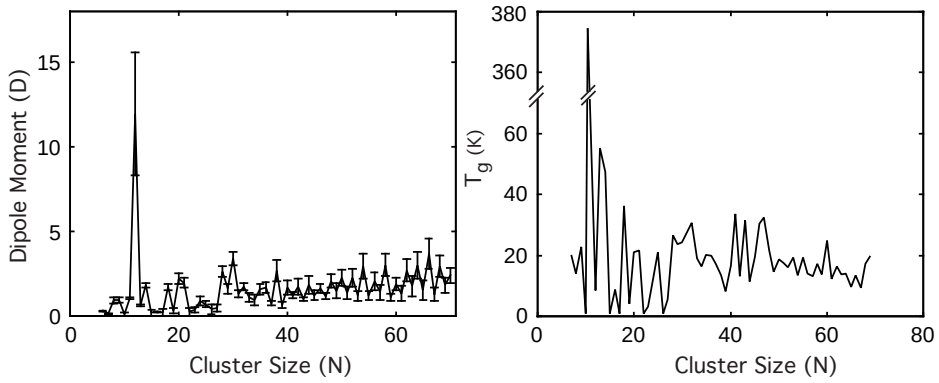

Figure 34: Electric dipole moments and transition temperatures of Nb clusters using two-component fitting.

REFERENCES

[1] Abd El Rahim, M., Antoine, R., Arnaud, L., Barbaire, M., Broyer, M., Clavier, C., Compagnon, I., Dugourd, P., Maurelli, J., and Rayane, D., "Position sensitive detection coupled to high-resolution time-of-flight mass spectrometry: Imaging for molecular beam deflection experiments," *Rev. Sci. Instrum.*, vol. 75, no. 12, pp. 5221–5227, 2004.

[2] Abrikosov, A. A. and Gorkov, L. P., "Contribution to the theory of superconducting alloys with paramagnetic impurities," *Soviet Phys-JETP*, vol. 12, p. 1243, 1961.

[3] Adams, E., "A new permanent magnet from powdered manganese bismuthide," *Rev. Mod. Phys.*, vol. 25, no. 1, pp. 306–309, 1953.

[4] Alameddin, G., Hunter, J., Cameron, D., and Kappes, M. M., "Electronic and geometric structure in silver clusters," *Chem. Phys. Lett.*, vol. 192, no. 1, pp. 122–128, 1992.

[5] Allen, P. B., Abanov, A. G., and Requist, R., "Quantum electrical dipole in triangular systems: A model for spontaneous polarity in metal clusters," *Phys. Rev. A*, vol. 71, no. 4, 2005.

[6] Andersen, K. E., Kumar, V., Kawazoe, Y., and Pickett, W. E., "Origin of spontaneous electric dipoles in homonuclear niobium clusters," *Phys. Rev. Lett.*, vol. 93, no. 24, 2004.

[7] Andersen, K. E., Kumar, V., Kawazoe, Y., and Pickett, W. E., "Origin of spontaneous electric dipoles in homonuclear niobium clusters (vol 93, art no 246105, 2004)," *Phys. Rev. Lett.*, vol. 95, no. 8, p. 246105, 2005.

[8] Anderson, P. W., "Theory of dirty superconductors," *J. Phys. Chem. Solids*, vol. 11, no. 1-2, pp. 26–30, 1959.

[9] Anderson, P. W., "Localized magnetic states in metals," *Phys. Rev.*, vol. 1, no. 1, p. 41, 1961.

[10] Anderson, P. W., "More is different - broken symmetry and nature of hierarchical structure of science," *Science*, vol. 177, no. 4047, p. 393, 1972.

[11] Bardeen, J., Cooper, L. N., and Schrieffer, J. R., "Theory of superconductivity," *Phys. Rev.*, vol. 108, p. 1175, 1957.

[12] Batista, C. D., Gubernatis, J. E., Bonca, J., and Lin, H. Q., "Intermediate coupling theory of electronic ferroelectricity," *Phys. Rev. Lett.*, vol. 92, no. 18, 2004.

[13] Beck, D. E., "Self-consistent calculation of the polarizability of small jellium spheres," *Phys. Rev. B*, vol. 30, no. 12, pp. 6935–6942, 1984.

[14] Bergeron, D. E., Roach, P. J., Castleman, A. W., Jones, N., and Khanna, S. N., "Al cluster superatoms as halogens in polyhalides and as alkaline earths in iodide salts," *Science*, vol. 307, no. 5707, pp. 231–235, 2005.

[15] Bernholc, J. and Phillips, J. C., "Kinetics of cluster formation in the laser vaporization source - carbon clusters," *J. Chem. Phys.*, vol. 85, no. 6, pp. 3258–3267, 1986.

[16] Bertsch, G., Onishi, N., and Yabana, K., "Magnetization of ferromagnetic clusters," *Z. Phys. D*, vol. 34, no. 3, pp. 213–217, 1995.

[17] Bertsch, G. F. and Yabana, K., "Cold cluster ferromagnetism," *Phys. Rev. A*, vol. 49, no. 3, pp. 1930–1932, 1994.

[18] Billas, I. M. L., Chatelain, A., and de Heer, W. A., "Magnetism from the atom to the bulk in iron, cobalt, and nickel clusters," *Science*, vol. 265, no. 5179, pp. 1682–1684, 1994.

[19] Black, C. T., Ralph, D. C., and Tinkham, M., "Spectroscopy of the superconducting gap in individual nanometer-scale aluminum particles," *Phys. Rev. Lett.*, vol. 76, no. 4, pp. 688–691, 1996.

[20] Bohr, A., Mottelson, B. R., and Pines, D., "Possible analogy between the excitation spectra of nuclei and those of the superconducting metallic state," *Phys. Rev.*, vol. 110, no. 4, pp. 936–938, 1958.

[21] Brack, M., "The physics of simple metal-clusters - self-consistent jellium model and semiclassical approaches," *Rev. Mod. Phys.*, vol. 65, no. 3, pp. 677–732, 1993.

[22] Braun, F. and von Delft, J., "Fixed-N superconductivity: The crossover from the bulk to the few-electron limit," *Phys. Rev. Lett.*, vol. 81, no. 21, pp. 4712–4715, 1998.

[23] Chervenak, J. A. and Valles, J. M., "Pair-breaking by magnetic-impurities in ultrathin superconducting films - T_c degradation mechanisms in disordered superconductors," *Phys. Rev. B*, vol. 51, no. 17, pp. 11977–11980, 1995.

[24] Chikazumi, S., *Physics of magnetism*. New York: Wiley, english ed., 1964.

[25] Clemenger, K., "Ellipsoidal shell structure in free-electron metal-clusters," *Phys. Rev. B*, vol. 32, no. 2, pp. 1359–1362, 1985.

[26] Coehoorn, R. and Degroot, R. A., "The electronic-structure of MnBi," *J. Phys. F: Met. Phys.*, vol. 15, no. 10, pp. 2135–2144, 1985.

[27] Cooper, L. N., "Bound electron pairs in a degenerate fermi gas," *Phys. Rev.*, vol. 104, p. 1189, 1956.

[28] Cox, A. J., Louderback, J. G., and Bloomfield, L. A., "Experimental-observation of magnetism in rhodium clusters," *Phys. Rev. Lett.*, vol. 71, no. 6, pp. 923–926, 1993.

[29] Cox, D. M., Trevor, D. J., Whetten, R. L., Rohlfing, E. A., and Kaldor, A., "Magnetic-behavior of free-iron and iron-oxide clusters," *Phys. Rev. B*, vol. 32, no. 11, pp. 7290–7298, 1985.

[30] Crangle, J., "The magnetization of cobalt-manganese and cobalt-chromium alloys," *Philos. Mag.*, vol. 2, no. 17, pp. 659–668, 1957.

[31] de Heer, W. A., "The physics of simple metal-clusters - experimental aspects and simple-models," *Rev. Mod. Phys.*, vol. 65, no. 3, pp. 611–676, 1993.

[32] de Heer, W. A. and Milani, P., "Large ion volume time-of-flight mass-spectrometer with position-sensitive and velocity-sensitive detection capabilities for cluster beams," *Rev. Sci. Instrum.*, vol. 62, no. 3, pp. 670–677, 1991.

[33] de Heer, W. A., Milani, P., and Chatelain, A., "Nonjellium-to-jellium transition in aluminum cluster polarizabilities," *Phys. Rev. Lett.*, vol. 63, no. 26, pp. 2834–2836, 1989.

[34] de Heer, W. A., Milani, P., and Chatelain, A., "Spin relaxation in small free iron clusters," *Phys. Rev. Lett.*, vol. 65, no. 4, pp. 488–491, 1990.

[35] de Heer, W. A., Selby, K., Kresin, V., Masui, J., Vollmer, M., Chatelain, A., and Knight, W. D., "Collective dipole oscillations in small sodium clusters," *Phys. Rev. Lett.*, vol. 59, no. 16, pp. 1805–1808, 1987.

[36] Dederichs, P. H., Zeller, R., Akai, H., and Ebert, H., "Abinitio calculations of the electronic-structure of impurities and alloys of ferromagnetic transition-metals," *J. Magn. Magn. Mater.*, vol. 100, no. 1-3, pp. 241–260, 1991.

[37] Dietl, T., "Ferromagnetic semiconductors," *Semicond. Sci. Technol.*, vol. 17, no. 4, pp. 377–392, 2002.

[38] Dietz, T. G., Duncan, M. A., Powers, D. E., and Smalley, R. E., "Laser production of supersonic metal cluster beams," *J. Chem. Phys.*, vol. 74, no. 11, pp. 6511–6512, 1981.

[39] Douglass, D. C., Cox, A. J., Bucher, J. P., and Bloomfield, L. A., "Magnetic-properties of free cobalt and gadolinium clusters," *Phys. Rev. B*, vol. 47, no. 19, pp. 12874–12889, 1993.

[40] Dugourd, P., Compagnon, I., Lepine, F., Antoine, R., Rayane, D., and Broyer, M., "Beam deviation of large polar molecules in static electric fields: theory and experiment," *Chem. Phys. Lett.*, vol. 336, no. 5-6, pp. 511–517, 2001.

[41] Ehrenreich, H. and M., S. L. in *Solid State Physics* (Ehrenreich, H., Seitz, F., and Turnbull, D., eds.), p. 149, New York: Academic, 1976.

[42] Ellialtioglu, S., Zeller, R., and Dederichs, P. H., "Magnetic 3d impurities in Nb and Mo," *J. Phys. F: Met. Phys.*, vol. 17, no. 2, pp. 409–416, 1987.

[43] Fa, W., Luo, C. F., and Dong, J. M., "Structure-dependent ferroelectricity of niobium clusters (Nb_N, N=2-52)," *Phys. Rev. B*, vol. 71, no. 24, 2005.

[44] Farges, J., Raoult, B., and Torchet, G., "Crystalline and noncrystalline effects in electron-diffraction patterns from small clusters in an argon cluster beam," *J. Chem. Phys.*, vol. 59, no. 7, pp. 3454–3458, 1973.

[45] Friedel, J., "The distribution of electrons round impurities in monovalent metals," *Philos. Mag.*, vol. 43, no. 337, pp. 153–189, 1952.

[46] Friedel, J., "Metallic alloys," *Nuovo Cimento Suppl.*, vol. 7, pp. 287–311, 1958.

[47] Furdyna, J. K., "Diluted magnetic semiconductors," *J. Appl. Phys.*, vol. 64, no. 4, pp. R29–R64, 1988.

[48] Gautier, F., "Itinerent magnetism," in *Magnetism of Metals and Alloys* (M, C., ed.), North-Holland Publishing Company, 1982.

[49] Gerion, D., *Thermal Properties of Ferromagnetic Clusters Studied in A Molecular Beam*. PhD thesis, EPFL, Lausanne, 1999.

[50] Gerion, D., Hirt, A., Billas, I., Chatelain, A., and de Heer, W. A., "Experimental specific heat of iron, cobalt, and nickel clusters studied in a molecular beam," *Phys. Rev. B*, vol. 62, pp. 7491–7501, 2000.

[51] Gerion, D., Hirt, A., and Chatelain, A., "High Curie temperature and possible canted magnetism in free Gd clusters," *Phys. Rev. Lett.*, vol. 83, no. 3, pp. 532–535, 1999.

[52] Ginsberg, D. M., "Depression of superconducting transition-temperature caused by 3d magnetic-impurities," *Phys. Rev. B*, vol. 10, no. 9, pp. 4044–4046, 1974.

[53] Gruner, G. and Zawadowski, A., "Magnetic-impurities in non-magnetic metals," *Rep. Prog. Phys.*, vol. 37, no. 12, pp. 1497–1583, 1974.

[54] Hamamoto, N., Onishi, N., and Bertsch, G., "Magnetic properties of an ensemble of rotating ferromagnetic clusters," *Phys. Rev. B*, vol. 61, no. 2, pp. 1336–1350, 2000.

[55] Hihara, T., Pokrant, S., and Becker, J. A., "Magnetic moments and chemical bonding in isolated Bi_NCo_M clusters," *Chem. Phys. Lett.*, vol. 294, no. 4-5, pp. 357–362, 1998.

[56] Himpsel, F. J., "Correlation between magnetic splitting and magnetic-moment for 3d transition-metals," *J. Magn. Magn. Mater.*, vol. 102, no. 3, pp. 261–265, 1991.

[57] Hirsch, J. E., "Charge expulsion and electric field in superconductors," *Phys. Rev. B*, vol. 68, no. 18, 2003.

[58] Ibach, H. and Leuth, H., *Solid-state physics : an introduction to principles of materials science*. Berlin; New York: Springer, 3rd ed., 2003.

[59] Ishida, K. and Nishizawa, T. in *Binary Alloy Phase Diagrams* (Massalski, T. B., ed.), ASM International, Materials Park, OH, 2nd ed., 1990.

[60] J., G. R. and A., P. P. L., *Chemical Bonding and Molecular Geometry from Lewis to Electron Densities*. New York: Oxford Univ. Press, 2001.

[61] Jackson, J. D., *Classical electrodynamics*. New York: Wiley, 3rd ed., 1999.

[62] Janssens, E., Neukermans, S., and Lievens, P., "Shells of electrons in metal doped simple metal clusters," *Curr. Opin. Solid St. M*, vol. 8, no. 3-4, pp. 185–193, 2004.

[63] Jarlborg, T. and Peter, M., "Electronic-structure, magnetism and Curie temperatures in Fe, Co and Ni," *J. Magn. Magn. Mater.*, vol. 42, no. 1, pp. 89–99, 1984.

[64] Kacman, P., "Spin interactions in diluted magnetic semiconductors and magnetic semiconductor structures," *Semicond. Sci. Technol.*, vol. 16, no. 4, pp. R25–R39, 2001.

[65] Katakuse, I., Ichihara, T., Fujita, Y., Matsuo, T., Sakurai, T., and Matsud, H., "Mass distributions of copper, silver and gold clusters and electronic shell structure," *Int. J. Mass Spectrom. Ion Processes*, vol. 67, no. 2, pp. 229–236, 1985.

[66] Khanna, S. N. and Linderoth, S., "Magnetic-behavior of clusters of ferromagnetic transition-metals," *Phys. Rev. Lett.*, vol. 67, no. 6, pp. 742–745, 1991.

[67] Khanna, S. N., Rao, B. K., Jena, P., and Knickelbein, M., "Ferrimagnetism in Mn_7 cluster," *Chem. Phys. Lett.*, vol. 378, no. 3-4, pp. 374–379, 2003.

[68] Kim, Y. J. and Overhauser, A. W., "Magnetic-impurities in superconductors - a theory with different predictions," *Phys. Rev. B*, vol. 49, no. 22, pp. 15799–15812, 1994.

[69] Kittel, C., *Introduction to solid state physics*. New York: Wiley, 7th ed., 1996.

[70] Knickelbein, M. B., "Experimental observation of superparamagnetism in manganese clusters," *Phys. Rev. Lett.*, vol. 86, no. 23, pp. 5255–5257, 2001.

[71] Knickelbein, M. B., "Magnetic ordering in manganese clusters," *Phys. Rev. B*, vol. 70, no. 1, p. 014424, 2004.

[72] Knickelbein, M. B. and Yang, S., "Photoionization studies of niobium clusters - ionization-potentials for Nb_2-Nb_{76}," *J. Chem. Phys.*, vol. 93, no. 8, pp. 5760–5767, 1990.

[73] Knickelbein, M. B., "Electronic shell structure in the ionization potentials of copper clusters," *Chem. Phys. Lett.*, vol. 192, no. 1, pp. 129–134, 1992.

[74] Knickelbein, M. B., "Magnetic ordering in clusters of the group 3 transition elements: Sc_n , Y_n , and La_n," *Phys. Rev. B*, vol. 71, no. 18, p. 184442, 2005.

[75] Knight, W. D., Clemenger, K., Deheer, W. A., and Saunders, W. A., "Polarizability of alkali clusters," *Phys. Rev. B*, vol. 31, no. 4, pp. 2539–2540, 1985.

[76] Knight, W. D., Clemenger, K., Deheer, W. A., Saunders, W. A., Chou, M. Y., and Cohen, M. L., "Electronic shell structure and abundances of sodium clusters," *Phys. Rev. Lett.*, vol. 52, no. 24, pp. 2141–2143, 1984.

[77] Knight, W. D., Monot, R., Dietz, E. R., and George, A. R., "Stern-Gerlach deflection of metallic-cluster beams," *Phys. Rev. Lett.*, vol. 40, no. 20, pp. 1324–1326, 1978.

[78] Koretsky, G. M., Kerns, K. P., Nieman, G. C., Knickelbein, M. B., and Riley, S. J., "Reactivity and photoionization studies of bimetallic cobalt-manganese clusters," *J. Phys. Chem. A*, vol. 103, no. 13, pp. 1997–2006, 1999.

[79] Koretsky, G. M. and Knickelbein, M. B., "Photoionization studies of manganese clusters: Ionization potentials for Mn_7 to Mn_{64}," *J. Chem. Phys.*, vol. 106, no. 23, pp. 9810–9814, 1997.

[80] Kroto, H. W., Heath, J. R., Obrien, S. C., Curl, R. F., and Smalley, R. E., "C_{60} - Buckminsterfullerene," *Nature*, vol. 318, no. 6042, pp. 162–163, 1985.

[81] Kubo, R., "Statistical-mechanical theory of irreversible processes .1. general theory and simple applications to magnetic and conduction problems," *J. Phys. Soc. Jpn.*, vol. 12, no. 6, pp. 570–586, 1957.

[82] Kunz, A. B. and Ginsberg, D. M., "Band calculation of the effect of magnetic impurity atoms on the properties of superconductors," *Phys. Rev. B*, vol. 22, no. 7, pp. 3165–3172, 1980.

[83] L., B. I. M., *Magnetism of Iron, Cobalt and Nickel Clusters Studied in Molecular Beams*. PhD thesis, EPFL, Lausanne, 1995.

[84] Landman, U., "Materials by numbers: Computations as tools of discovery," *Proc. Natl. Acad. Sci. U. S. A.*, vol. 102, no. 19, pp. 6671–6678, 2005.

[85] Lang, P., Drittler, B., Zeller, R., and Dederichs, P. H., "Magnetic 3d impurities in Nb and Mo revisited," *J. Phys.: Condens. Matter*, vol. 4, no. 3, pp. 911–918, 1992.

[86] Li, X. and Wang, L. S., "Experimental search and characterization of icosahedral clusters: $Al_{12}X^-$ (X=C, Ge, Sn, Pb)," *Phys. Rev. B*, vol. 65, no. 15, p. 153404, 2002.

[87] Malozemoff, A. P., Williams, A. R., and Moruzzi, V. L., ""band-gap theory" of strong ferromagnetism: Application to concentrated crystalline and amorphous Fe- and Co-metalloid alloys," *Phys. Rev. B*, vol. 29, no. 4, pp. 1620–1632, 1984.

[88] Malozemoff, A. P., Williams, A. R., Moruzzi, V. L., and Terakura, K., "Energy-band analysis of ordered Fe and Co compounds - implications for amorphous ferromagnets," *Phys. Rev. B*, vol. 30, no. 11, pp. 6565–6572, 1984.

[89] Malozemoff, A. P., Williams, A. R., Terakura, K., Moruzzi, V. L., and Fukamichi, K., "Magnetism of amorphous metal metal-alloys," *J. Magn. Magn. Mater.*, vol. 35, no. 1-3, pp. 192–198, 1983.

[90] Matthias, B. T., E., S., and E., C., "Spin exchange in superconductors," *Phys. Rev. Lett.*, vol. 1, no. 3, pp. 92–94, 1958.

[91] Matthias, B. T., Suhl, H., and Corenzwit, E., "Ferromagnetic superconductors," *Phys. Rev. Lett.*, vol. 1, no. 12, pp. 449–450, 1958.

[92] Matveev, K. A. and Larkin, A. I., "Parity effect in ground state energies of ultrasmall superconducting grains," *Phys. Rev. Lett.*, vol. 78, no. 19, pp. 3749–3752, 1997.

[93] Morisato, T., Khanna, S. N., and Kawazoe, Y., "First-principles study of the onset of noncollinearity in Mn_n clusters: Magnetic arrangements in Mn_5 and Mn_6," *Phys. Rev. B*, vol. 72, p. 014435, 2005.

[94] Moro, R., Xu, X. S., Yin, S. Y., and de Heer, W. A., "Ferroelectricity in free niobium clusters," *Science*, vol. 300, no. 5623, pp. 1265–1269, 2003.

[95] Moro, R., Yin, S. Y., Xu, X. S., and de Heer, W. A., "Spin uncoupling in free Nb clusters: Support for nascent superconductivity," *Phys. Rev. Lett.*, vol. 93, no. 8, p. 086803, 2004.

[96] Moro, R. A., *Ferroelectricity in Free Niobium Clusters*. PhD thesis, Georgia Institute of Technology, 2003.

[97] Mott, N. F., "Metal-insulator transition," *Rev. Mod. Phys.*, vol. 40, no. 4, p. 677, 1968.

[98] Nayak, S. K. and Jena, P., "Anomalous magnetism in small Mn clusters," *Chem. Phys. Lett.*, vol. 289, no. 5-6, pp. 473–479, 1998.

[99] Neukermans, S., Janssens, E., Chen, Z. F., Silverans, R. E., Schleyer, P. V., and Lievens, P., "Extremely stable metal-encapsulated $AlPb_{10}^+$ and $AlPb_{12}^+$ clusters: Mass-spectrometric discovery and density functional theory study," *Phys. Rev. Lett.*, vol. 92, no. 16, 2004.

[100] Nonose, S., Sone, Y., and Kaya, K., "Reactivity and stability of bimetallic clusters," *Z. Phys. D*, vol. 19, no. 1-4, pp. 357–359, 1991.

[101] Nonose, S., Sone, Y., Onodera, K., Sudo, S., and Kaya, K., "Structure and reactivity of bimetallic Co_nV_m clusters," *J. Phys. Chem.*, vol. 94, no. 7, pp. 2744–2746, 1990.

[102] O'Handley, R. C., *Modern Magnetic Materials: Principles and Applications*. New York: Wiley, 2000.

[103] Ohno, H., Chiba, D., Matsukura, F., Omiya, T., Abe, E., Dietl, T., Ohno, Y., and Ohtani, K., "Electric-field control of ferromagnetism," *Nature*, vol. 408, no. 6815, pp. 944–946, 2000.

[104] Ovchinnikov, Y. N. and Kresin, V. Z., "Giant strengthening of superconducting pairing in metallic nanoclusters," *Eur. Phys. J. B*, pp. 5–7, 2005.

[105] Ovchinnikov, Y. N. and Kresin, V. Z., "Strong pair correlation in small metallic nanoclusters: the energy spectrum," *Eur. Phys. J. B*, vol. 47, no. 3, pp. 333–336, 2005.

[106] Papanikolaou, N., Stefanou, N., Zeller, R., and Dederichs, P. H., "Local spin moments of transition-metal impurities in monovalent simple-metal hosts," *Phys. Rev. B*, vol. 46, no. 17, pp. 10858–10865, 1992.

[107] Pauling, L., "The nature of the interatomic forces in metals," *Phys. Rev.*, vol. 54, no. 11, pp. 899–904, 1938.

[108] Pauly, H., *Atom, Molecule, and Cluster Beams*, vol. 2. Berlin ; New York: Springer.

[109] Pederson, M. R., Reuse, F., and Khanna, S. N., "Magnetic transition in Mn_n (n=2-8) clusters," *Phys. Rev. B*, vol. 58, no. 9, pp. 5632–5636, 1998.

[110] Pokrant, S., Herwig, C., Hihara, T., and Becker, J. A., "Electronic spin-spin coupling in rare earth doped semiconductor and semimetal clusters," *Eur. Phys. J. D*, vol. 9, no. 1-4, pp. 509–512, 1999.

[111] Rado, G. T. and Suhl, H., *Magnetism*. New York: Academic Press, 1963.

[112] Ralph, D. C., Gueron, S., Black, C. T., and Tinkham, M., "Electron energy levels in superconducting and magnetic nanoparticles," *Physica B*, vol. 280, no. 1-4, pp. 420–424, 2000.

[113] Ramsey, N., *Molecular Beams*. Oxford: Clarendon Press, 1956.

[114] Rodriguez-Lopez, J. L., Aguilera-Granja, F., Michaelian, K., and Vega, A., "Structure and magnetism of cobalt clusters," *Phys. Rev. B*, vol. 67, no. 17, p. 174413, 2003.

[115] Rohlfing, E. A., Cox, D. M., Petkovicluton, R., and Kaldor, A., "Alloy cluster beams - nickel/chromium and nickel/aluminum," *J. Phys. Chem.*, vol. 88, no. 25, pp. 6227–6231, 1984.

[116] Roy, A., Buchanan, D. S., Holmgren, D. J., and Ginsberg, D. M., "Localized magnetic-moments on chromium and manganese dopant atoms in niobium and vanadium," *Phys. Rev. B*, vol. 31, no. 5, pp. 3003–3014, 1985.

[117] Sanchez, A., Abbet, S., Heiz, U., Schneider, W. D., Hakkinen, H., Barnett, R. N., and Landman, U., "When gold is not noble: Nanoscale gold catalysts," *J. Phys. Chem. A*, vol. 103, no. 48, pp. 9573–9578, 1999.

[118] Schechter, M., von Delft, J., Imry, Y., and Levinson, Y., "Two pairing parameters in superconducting grains," *Phys. Rev. B*, vol. 67, no. 6, p. 064506, 2003.

[119] Schmidt, M., Kusche, R., Kronmuller, W., vonIssendorff, B., and Haberland, H., "Experimental determination of the melting point and heat capacity for a free cluster of 139 sodium atoms," *Phys. Rev. Lett.*, vol. 79, no. 1, pp. 99–102, 1997.

[120] Sherrill, M. D. and Edwards, H. H., "Superconducting tunneling on bulk niobium," *Phys. Rev. Lett.*, vol. 6, no. 9, p. 460, 1961.

[121] Slater, J. C., "Electronic structure of alloys," *J. Appl. Phys.*, vol. 8, no. 6, pp. 385–390, 1937.

[122] Snider, D. R. and Sorbello, R. S., "Density-functional calculation of the static electronic polarizability of a small metal sphere," *Phys. Rev. B*, vol. 28, no. 10, pp. 5702–5710, 1983.

[123] Sone, Y., Hoshino, K., Naganuma, T., Nakajima, A., and Kaya, K., "Production of bimetallic clusters containing manganese atoms by laser-vaporization method," *J. Phys. Chem.*, vol. 95, no. 18, pp. 6830–6832, 1991.

[124] Stekly, Z. J. J. and Gregory, E., *Magnetic, Electrical and Optical Properties and Applications of Intermetallic Compounds*, vol. 4 of *Intermetallic Compounds*. John Wiley & Sons, 2000.

[125] Stepanyuk, V. S., Zeller, R., Dederichs, P. H., and Mertig, I., "Electronic-structure and magnetic-properties of dilute Co alloys with transition-metal impurities," *Phys. Rev. B*, vol. 49, no. 8, pp. 5157–5164, 1994.

[126] Tanigaki, K., Hirosawa, I., Ebbesen, T. W., Mizuki, J., Shimakawa, Y., Kubo, Y., Tsai, J. S., and Kuroshima, S., "Superconductivity in sodium-containing and lithium-containing alkali-metal fullerides," *Nature*, vol. 356, no. 6368, pp. 419–421, 1992.

[127] Terakura, K. and Kanamori, J., "Calculation of electronic structure of an impurity atom of non-transition element in nickel," *Prog. Theor. Phys.*, vol. 46, no. 4, p. 1007, 1971.

[128] Tinkham, M., *Introduction to superconductivity*. New York: McGraw Hill, 2nd ed., 1996.

[129] Torres, M., Fernandez, E., and Balbas, L., "Theoretical study of structural, electronic, and magnetic properties of Au_nM^+ clusters (M=Sc, Ti, V, Cr, Mn, Fe, Au; n <= 9)," *Phys. Rev. B*, vol. 71, no. 15, p. 155412, 2005.

[130] Toshima, N. and Yonezawa, T., "Bimetallic nanoparticles novel materials for chemical and physical applications," *New J. Chem.*, vol. 22, no. 11, pp. 1179–1201, 1998.

[131] van der Marel, D., Sawatzky, G. A., and Hillebrecht, F. U., "Direct observation of the exchange-split virtual bound-state in dilute Mn alloys," *Phys. Rev. Lett.*, vol. 53, no. 2, pp. 206–209, 1984.

[132] Van Vleck, J. H., "Quantum mechanics - the key to understanding magnetism," *Rev. Mod. Phys.*, vol. 50, no. 2, p. 191, 1978.

[133] Visuthikraisee, V. and Bertsch, G. F., "Spin-rotation coupling in ferromagnetic clusters," *Phys. Rev. A*, vol. 54, no. 6, pp. 5104–5109, 1996.

[134] von Issendorff, B. and Cheshnovsky, O., "Metal to insulator transitions in clusters," *Annu. Rev. Phys. Chem.*, vol. 56, no. 1, pp. 549–580, 2005.

[135] Wang, Q., Sun, Q., Yu, J. Z., Zeng, Z., and Kawazoe, Y., "The local magnetism of Fe impurity in Nb_n and Nb_nMo_m clusters," *J. Magn. Magn. Mater.*, vol. 184, no. 1, pp. 106–110, 1998.

[136] Whetten, R. L., Khoury, J. T., Alvarez, M. M., Murthy, S., Vezmar, I., Wang, Z. L., Stephens, P. W., Cleveland, C. L., Luedtke, W. D., and Landman, U., "Nanocrystal gold molecules," *Advanced Materials*, vol. 8, no. 5, p. 428, 1996.

[137] Williams, A. R., Malozemoff, A. P., Moruzzi, V. L., and Matsui, M., "Transition between fundamental magnetic behaviors revealed by generalized Slater-Pauling construction," *J. Appl. Phys.*, vol. 55, no. 6, pp. 2353–2355, 1984.

[138] Williams, A. R., Moruzzi, V. L., Malozemoff, A. P., and Terakura, K., "Generalized Slater-Pauling curve for transition-metal magnets," *IEEE Trans. Magn.*, vol. 19, no. 5, pp. 1983–1988, 1983.

[139] Wilson, A. H., "The theory of electronic semi-conductors," *Proc. R. Soc. London, A*, vol. 133, no. 822, pp. 458–491, 1931.

[140] Wolff, P. A., "Localized moments in metals," *Phys. Rev.*, vol. 124, no. 4, p. 1030, 1961.

[141] Wrigge, G., Hoffmann, M. A., and von Issendorff, B., "Photoelectron spectroscopy of sodium clusters: Direct observation of the electronic shell structure," *Phys. Rev. A*, vol. 65, no. 6, 2002.

[142] Wrigge, G., Hoffmann, M., von Issendorff, B., and Haberland, H., "Ultraviolet photoelectron spectroscopy of Nb_4^- to Nb_{200}^-," *European Phys. J. B*, vol. 24, pp. 23–26, 2003.

[143] Xu, S., Moritomo, Y., Kato, K., and Nakamura, A., "Mn-substitution effects on MgB_2 superconductor," *J. Phys. Soc. Jpn.*, vol. 70, no. 7, pp. 1889–1891, 2001.

[144] Xu, X. S. Unpublished.

[145] Xu, X. S., Yin, S. Y., Moro, R., and de Heer, W. A., "Magnetic moments and adiabatic magnetization of free cobalt clusters," *Phys. Rev. Lett.*, vol. 95, no. 23, p. 237209, 2005.

[146] Yazdani, A., Jones, B. A., Lutz, C. P., Crommie, M. F., and Eigler, D. M., "Probing the local effects of magnetic impurities on superconductivity," *Science*, vol. 275, no. 5307, pp. 1767–1770, 1997.

[147] Yin, S. Y., Xu, X. S., Moro, R., and de Heer, W. A., "Measurement of magnetic moments of free Bi_NMn_M clusters," *Phys. Rev. B*, vol. 72, no. 17, p. 174410, 2005.

[148] Young, B. A., Saab, T., Cabrera, B., Cross, J. J., Clarke, R. M., and Abusaidi, R. A., "Measurement of T_c suppression in tungsten using magnetic impurities," *J. Appl. Phys.*, vol. 86, no. 12, pp. 6975–6978, 1999.

[149] Zeller, R., "Local magnetic-behavior of transition-metal impurities in nickel," *J. Phys. F: Met. Phys.*, vol. 17, no. 10, pp. 2123–2137, 1987.

[150] Ziock, K. P., *Molecular Beam Studies of the Magnetic Moments of Small Metal Particles*. PhD thesis, Stanford University, 1985.

[151] Zitoun, D., Respaud, M., Fromen, M. C., Casanove, M. J., Lecante, P., Amiens, C., and Chaudret, B., "Magnetic enhancement in nanoscale CoRh particles," *Phys. Rev. Lett.*, vol. 89, no. 3, p. 037203, 2002.

[152] Zitoun, D., Respaud, M., Fromen, M. C., Lecante, P., Casanove, M., Amiens, C., and Chaudret, B., "Bimetallic CoRh and CoRu nanoparticles: size-induced enhanced magnetisation," *J. Magn. Magn. Mater.*, vol. 272-76, pp. 1536–1538, 2004.

VITA

Shuangye Yin was born in his lovely hometown of Dagang, in Zhenjiang City, Jiansu Province, China. He went to Nanjing University in 1993 and stayed there until he received his B.S. degree in 1997 and M.S. degree in 2000. His research interests there were computer simulations on metal clusters and nanowires. He went to Georgia Tech in Fall 2000 and joined Prof. Walter de Heer's group, where he learned molecular-beam methods to study atomic clusters. His research involves electronic and magnetic properties of clusters, especially alloy clusters.